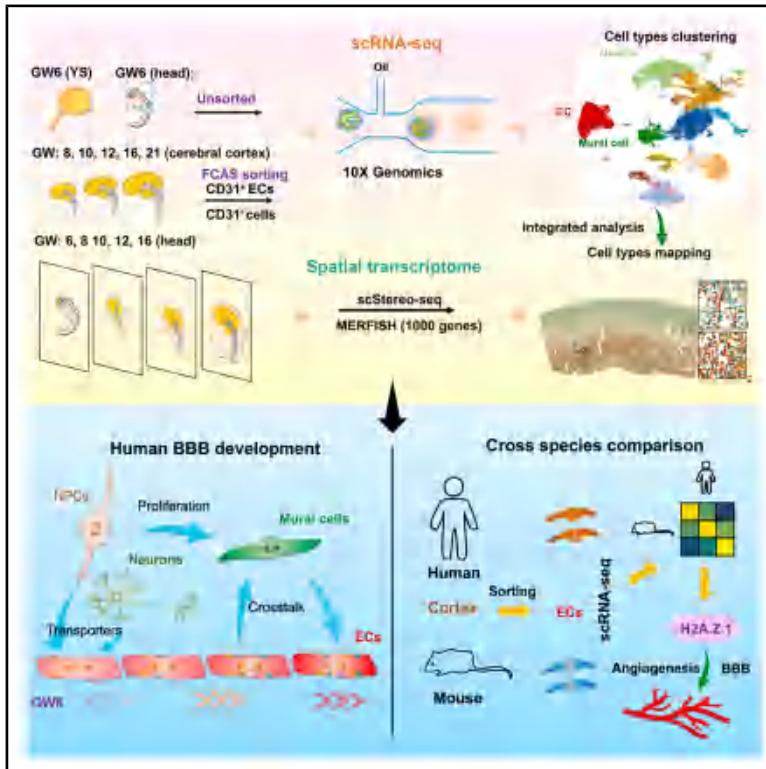


Cell Stem Cell

Decoding the spatiotemporal development of the blood-brain barrier in human cortex

Graphical abstract



Authors

Zhongqiu Li, Yanxin Li, Ziqing He, ..., Peng Du, Ji Dong, Jianwei Jiao

Correspondence

liyanxin@ioz.ac.cn (Y.L.),
dong_ji@gzlab.ac.cn (J.D.),
jwjiao@ioz.ac.cn (J.J.)

In brief

Our study systematically reveals the initiation and establishment of the human blood-brain barrier (BBB) using spatiotemporal transcriptomics. By comparing human and mouse BBB development, we demonstrate the evolutionary conservation of this process and identify H2A.Z.1 as a key protein for BBB development.

Highlights

- Spatiotemporal transcriptome defines NVU-related cell types during BBB development
- Neural cells induce BBB-specific transporter expression via CADHERIN-2 (*CDH2*)-mediated signaling
- Neural progenitor cells promote the proliferation of mural cells
- H2A.Z.1 regulates angiogenesis and BBB development

Resource

Decoding the spatiotemporal development of the blood-brain barrier in human cortex

Zhongqiu Li,^{1,2,3,4,16} Yanxin Li,^{1,2,3,5,16,*} Ziqing He,^{6,7,16} Changliang Wang,⁶ Yuehong Zhang,⁸ Rong Li,⁹ Lei Jin,¹⁰ Jin Jiao,¹¹ Fen Ji,^{1,2,3} Bing Zhu,^{12,13} Jingjing Zhang,¹⁴ Peng Du,¹⁵ Ji Dong,^{6,*} and Jianwei Jiao^{1,2,3,17,*}

¹State Key Laboratory of Organ Regeneration and Reconstruction, Institute of Zoology, Chinese Academy of Sciences, Beijing 100101, China

²Medical School, University of Chinese Academy of Sciences, Beijing 100049, China

³Beijing Institute for Stem Cell and Regenerative Medicine, Beijing 100101, China

⁴Fifth Affiliated Hospital of Zhengzhou University, Zhengzhou 400015, China

⁵State Key Laboratory of Common Mechanism Research for Major Diseases, Department of Cell Biology, Institute of Basic Medical Sciences & School of Basic Medicine, Chinese Academy of Medical Sciences & Peking Union Medical College, Beijing 100005, China

⁶Guangzhou National Laboratory, Guangzhou 510005, China

⁷Faculty of Health Sciences and UM-Bioland Joint Laboratory, University of Macau, Macau 999078, China

⁸Tongzhou Maternal and Child Health Hospital of Beijing, Beijing 101100, China

⁹Beijing Key Laboratory of Reproductive Endocrinology and Assisted Reproductive Technology and Key Laboratory of Assisted Reproduction, Department of Obstetrics and Gynecology, Ministry of Education, Center for Reproductive Medicine, Peking University Third Hospital, Beijing 100191, China

¹⁰Institute of Reproductive and Child Health, Peking University, National Health Commission Key Laboratory, Peking University, Beijing 100191, China

¹¹School of Basic Medicine, Medical Science and Technology Innovation Center, Shandong First Medical University & Shandong Academy of Medical Sciences, Jinan 250117, China

¹²Center for Translational Neurodegeneration and Regenerative Therapy, Tongji Hospital Affiliated to Tongji University, Shanghai, China

¹³Department of Neurology, Tongji Hospital Affiliated to Tongji University, Shanghai, China

¹⁴Affiliated Hospital of Guangdong Medical University, Zhanjiang 524001, China

¹⁵MOE Key Laboratory of Cell Proliferation and Differentiation, School of Life Sciences, Peking University, Beijing 100871, China

¹⁶These authors contributed equally

¹⁷Lead contact

*Correspondence: liyanxin@ioz.ac.cn (Y.L.), dong_ji@gzlab.ac.cn (J.D.), jwjiao@ioz.ac.cn (J.J.)

<https://doi.org/10.1016/j.stem.2026.02.010>

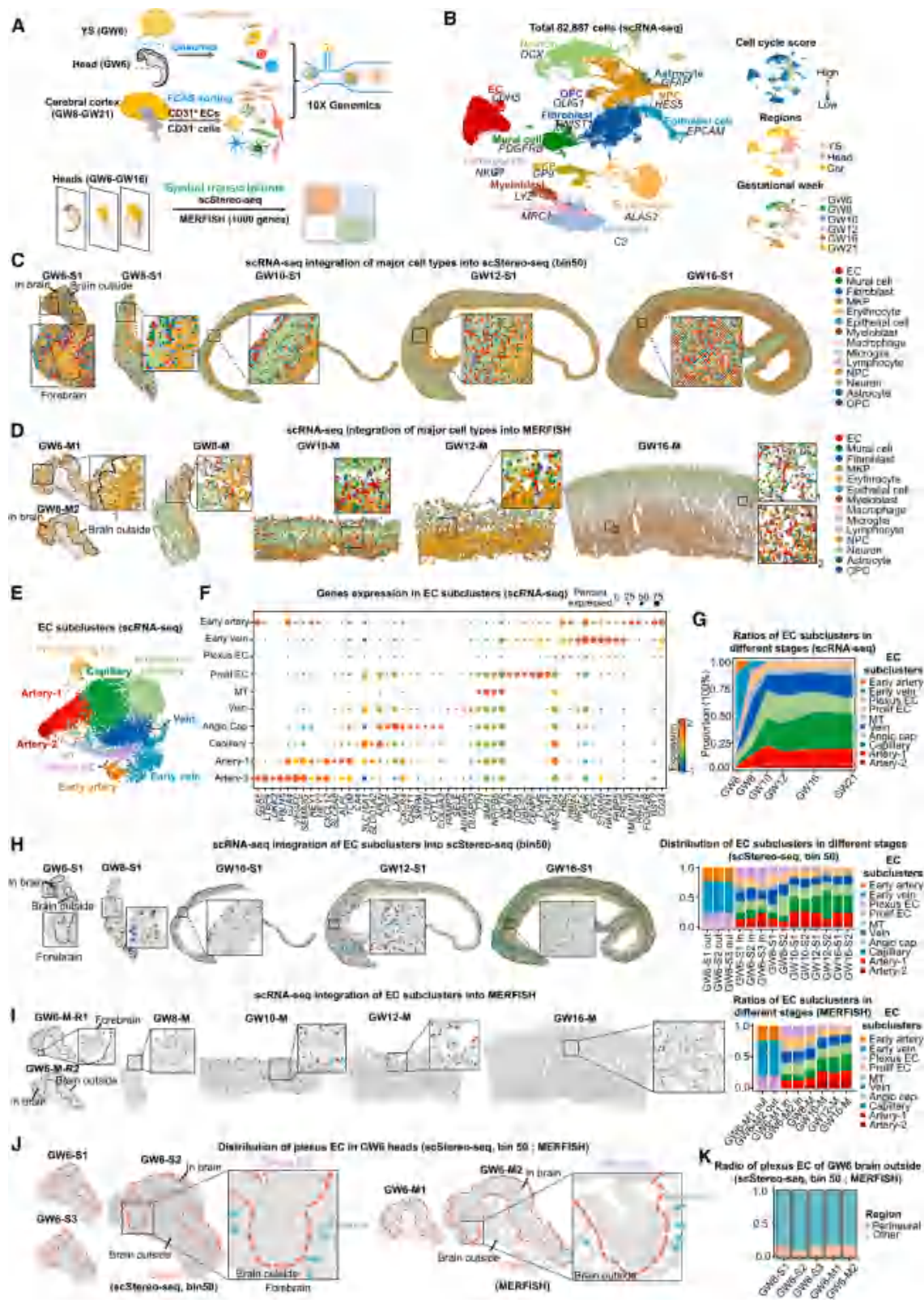
SUMMARY

The blood-brain barrier (BBB) is essential for maintaining the homeostasis of the central nervous system. However, the processes of BBB formation in humans remain unclear. Here, using single-cell spatiotemporal transcriptomics, we investigate human BBB development from 6 to 21 gestational weeks (GWs) and observe widespread expression of BBB-specific transporters in all brain-endothelial subclusters during development. We determine the onset of the human BBB-like transcriptional signature at GW8 and prove that neural cells can induce the expression of BBB-specific transporters in brain endothelial cells (ECs) via *CADHERIN-2 (CDH2)*. We also demonstrate that neural progenitor cells promote the proliferation of mural cells. Concomitant with the initiation of the BBB-like transcriptional signature, communication signals between ECs and mural cells begin to intensify. In addition, we reveal conserved BBB development between humans and mice and demonstrate that *H2A.Z.1* regulates angiogenesis and BBB development. Collectively, these findings provide unique insights into understanding human BBB ontogeny and identifying therapeutic targets for BBB-related disorders.

INTRODUCTION

The realization of blood-brain barrier (BBB) functions depends on the special multicellular structure called the neurovascular unit (NVU), which includes endothelial cells (ECs), mural cells, neural cells, and glial cells (in particular, astrocytes), among others.¹ However, due to the complexity of multi-cellular interactions, fully understanding the establishment process of the BBB remains a huge challenge.

In mouse studies, it was found that neural progenitor cells (NPCs) can regulate the vascularization of the CNS via the Wnt/ β -catenin pathway.^{2,3} Previous studies in humans have characterized brain vascular cells across development, adulthood, and disease.⁴⁻⁷ However, it remains unclear how the BBB is established in the human brain. Therefore, comprehensive and systematic investigations are required to understand the initiation, dynamics, characteristics, and spatial distribution of these cell types during human BBB development.



(legend on next page)

Single-cell spatial enhanced-resolution omics sequencing (scStereo-seq) has proven to be a powerful tool for understanding human BBB development.^{8,9} Meanwhile, multiplexed error-robust fluorescence *in situ* hybridization (MERFISH) offers robust capabilities for dissecting the refined structure of the BBB.^{10,11}

In this study, we constructed a comprehensive spatiotemporal transcriptomic atlas of the human BBB from 6 to 21 gestational weeks (GWs) by combining single-cell RNA sequencing (scRNA-seq) and spatial transcriptomics (scStereo-seq and MERFISH) technologies. We classified NVU-related cell types and explored their dynamic changes, interactions, and contributions to BBB development.

RESULTS

Single-cell spatiotemporal transcriptomic atlas of human BBB development

To study human BBB development, we first profiled single-cell transcriptomes of the yolk sac and head tissues at GW6 (Carnegie stage 12 [CS12]), as well as cerebral cortices at multiple GWs (i.e., GW8, GW10, GW12, GW16, and GW21) from 11 human embryos. Due to the low proportion of ECs, we utilized fluorescence-activated cell sorting (FACS) to enrich CD31⁺ ECs and sequenced both CD31⁺ ECs and other CD31⁻ cells (Figures 1A and S1A; Table S1). After strict quality control and batch-effect correction by Harmony,¹² 82,887 cells were profiled and grouped into 14 major cell types, with high correlation similarities between samples of the same stages and tissue types (Figures 1B and S1B–S1E). According to classic marker genes, they were identified as ECs (*CDH5*), mural cells (*PDGFRB*), fibroblasts (*TWIST1*), epithelial cells (*EPCAM*), megakaryocyte progenitors (MKPs; *GP9*), erythrocytes (*ALAS2*), myeloblasts (*LYZ*), macrophages (*MRC1*), microglia (*C3*), lymphocytes (*NKG7*), NPCs (*HES5*), astrocytes (*GFAP*), oligodendrocyte precursor cells (OPCs; *OLIG1*), and neurons (*DCX*) (Figures 1B, S1F, and S1G; Table S2).

To determine the spatial localization of these cell types in the cerebral cortex, we used Tangram¹³ to map them onto our published human brain scStereo-seq data,⁹ (Figures 1C and S1M; Table S3). In addition, to observe the more refined BBB structure of NVU-associated cell types, we also conducted MERFISH experiments. Both scStereo-seq and MERFISH were performed

across critical developmental stages (GW6–GW16) of the human BBB (Figure 1D; Tables S3 and S6). Quality control analysis revealed that not only do the respective biological replicate samples within each technology at the same time point exhibit high reproducibility, but there is also a high correlation between these two technologies at identical time points (Figures S1H–S1L). Overall, we constructed a spatiotemporal transcriptomic atlas of human BBB development at single-cell resolution.

Molecular characteristics of EC subclusters

As ECs are the core components of the NVU, we first explored their cell heterogeneity and reclustered them into ten subclusters (Figures 1E and S2A). Notably, we identified two extra-brain early EC subclusters, namely early artery and early vein ECs, which exhibited robust expression of tissue-remodeling regulators (*MDK* and *CD24*) yet lacked expression of the brain-specific endothelial marker *MFSD2A*.^{14–16} Meanwhile, we further characterized the precursor population of brain ECs: plexus ECs,¹⁷ termed plexus-like ECs,^{17–19} which initiated expression of *MFSD2A*. Our work confirmed its presence in human transcriptomic datasets.²⁰ In addition, we also characterized seven other brain EC subclusters. Proliferating ECs were distinguished by high expression of proliferation markers (*MKI67* and *UBE2C*).^{7,15,21} MT ECs showed pronounced enrichment of mitochondrial-associated genes (e.g., *TTN* and *SMG1*).⁷ Vein ECs highly expressed *ADGRG6*, *DUSP23*, and *SELE*, whereas angiogenic capillary ECs were marked by known marker genes (*PGF*, *LXN*, *CXCR4*, and *APLN*),^{7,21–24} as well as newly identified genes, such as *LY6H*, *CHST1*, and *CYTL1*. Capillary ECs highly expressed canonical capillary markers: *CA4*,^{25,26} *SLC16A1*,²⁷ and *SLCO1A2*.²¹ For arterial ECs, we identified two subclusters, artery-1 and artery-2 ECs, which expressed the arterial marker genes *GJA4* and *CXCL12*. Owing to the specific expression of *LTBP4*⁷ and *FBLN5*,¹⁶ artery-2 ECs were classified as a more mature subcluster (Figures 1F and S2B–S2D). Notably, highlighting these marker genes in the uniform manifold approximation and projection (UMAP) visualization demonstrated that these clusters represent pseudo-arbitrary distinctions (Figures 1E and S2B).

Spatiotemporal dynamic changes of EC subclusters

To investigate cortical vascularization, we first explored the spatiotemporal changes in EC subclusters. At GW6, early and

Figure 1. Spatiotemporal transcriptomic profiles of the developing human cerebrovasculature

(A) Schematic illustration of regions, periods, and study design of sequencing. For 10× Genomics scRNA-seq, FACS was applied to increase the proportion of CD31⁺ ECs in GW8–GW21 cerebral cortices. For the spatial transcriptome, GW6–GW16 heads were used for sequencing of scStereo-seq and MERFISH (1,000 genes). Details are shown in Table S1.

(B) Uniform manifold approximation and projection (UMAP) showing 82,887 cells, colored by clusters. The major cell types (left) are displayed in different colors, and the marker genes of each type are shown in italics. Three UMAPs (right), showing the information of cell cycle score, dissected region, and GW.

(C) Spatial visualization of major cell types at GW6–GW16 using scStereo-seq.

(D) Spatial visualization of major cell types at GW6–GW16 using MERFISH.

(E) UMAP visualization showing the re-clustered EC subclusters.

(F) Dot plot showing the marker genes used for identifying EC subclusters.

(G) Area chart showing proportion changes of different EC subclusters from GW6 to GW21.

(H) Spatial visualization of EC subclusters at GW6–GW16 using scStereo-seq. Bar plots displaying ratios of EC subclusters in different stages.

(I) Spatial visualization of EC subclusters at GW6–GW16 using MERFISH. Bar plots showing ratios of EC subclusters in different stages.

(J) Spatial visualization of distribution of plexus EC in GW6 heads by scStereo-seq and MERFISH.

(K) Bar plots displaying distribution of plexus EC of GW6 brain outside by scStereo-seq and MERFISH.

YS, yolk sac; EC, endothelial cell; NPC, neural progenitor cell; OPC, oligodendrocyte precursor cell; MKP, megakaryocyte progenitor; S, scStereo-seq; M, MERFISH; Prolif, proliferating; Angio cap, angiogenic capillary. See also Figures S1 and S2 and Tables S1, S2, S3, and S6.

plexus ECs accounted for the majority. From GW8 onward, the proportion of early ECs sharply declined, coinciding with the expansion of brain EC subclusters (Figure 1G). Based on the scRNA-seq data, we analyzed the developmental trajectory of the EC subclusters, wherein plexus ECs appeared earlier, while artery-2 ECs appeared later (Figures S2E–S2H). Interestingly, the developmental trajectory showed that plexus ECs first transitioned into venous ECs, which subsequently differentiated into two branches, namely angiogenic capillary and capillary/artery ECs, along with the cell proliferation process (Figures S2G and S2H).¹⁵

Moreover, spatial visualization further verified the existence of these EC subclusters and revealed that their proportion changes with development (Figures 1H, 1I, S2I, and S2J). Meanwhile, we also analyzed the distribution of plexus ECs outside the brain. As expected, plexus ECs were enriched in the perineural region (Figures 1J and 1K). These results indicate that human brain vascularization begins at GW6.

Characteristics of BBB initiation and development in human ECs

To explore the transcriptional characteristics of BBB initiation and development, we first detected the expression patterns of BBB-specific transporter-related genes²⁸ (Figure 2A; Table S5). Interestingly, these transporter-related genes were absent in extra-brain EC subclusters, and weakly expressed in plexus ECs. Strikingly, these genes were ubiquitously expressed in EC subclusters within the brain. Meanwhile, we also investigated these genes in a published adult human EC dataset.⁷ Notably, we found that these genes were weakly or barely expressed in the large artery subcluster, except for the ATP-binding cassette (ABC) family-related genes (Figure 2A).²⁹

Furthermore, we examined the expression score of BBB-specific transporter-related genes in EC subclusters at different stages, from GW5 to adult, using our data, the data from Zeng et al.,³⁰ and adult data from Wälchli et al.⁷ Temporal analysis of these gene scores across GW5–adulthood datasets revealed negligible expression at GW5–GW7, followed by obvious upregulation at GW8 (Figure 2B). Based on the spatial data, we verified the above results by lighting and scoring the transporter-related gene set (Figures 2C, 2D, and S3C–S3E). Finally, the

above conclusions were also validated by immunofluorescence staining (Figures 2E–2I).

In addition, proteins that are related to tight junction (TJ), adherens junction (AJ), and junctional adhesion molecule (JAM) also contribute to the physical barrier of the BBB.¹ We found that the expression levels of *CLDN5* in ECs inside the brain were higher than those outside the brain (Figure S3A). We found that the expression scores of TJ-related genes were low in EC subclusters from GW5 to GW7, whereas their expression scores exhibited a marked upregulation starting at GW8 (Figures S3B, S3C, S3D, and S3F). Meanwhile, we observed that transcytosis-associated gene expression scores were low at GW5, followed by a progressive increase commencing at GW6, with subsequent stabilization after GW10. Intriguingly, these genes remained highly expressed in adulthood (Figure S3B).^{14,28,31} Taken together, these results suggest that human brain ECs begin to acquire a BBB-like transcriptional signature from GW8.

Neural cells induce the expression of BBB-specific transporters in ECs via activation of the CDH2-CDH2 pathway

Neural cells have been reported to play indispensable roles in BBB development.^{28,32,33} To investigate whether different neural-cell-enriched regions had variant effects on BBB development, we divided the cerebral cortex into an NPC-enriched zone (NPZ, ventricular and subventricular zones) and a neuron-enriched zone (NZ, intermediate zone and cortical plate) (Figure S4A).³⁴ Spatial analysis revealed that, from GW6 to GW16, the proportion of neural cells was very high, and the adjacent cell types around ECs were mainly NPCs and neurons (Figures 3A, 3B, and S4B).

To understand how neural cells influence BBB development in ECs, we performed a cell-cell communication analysis between ECs and other major cell types³⁶ and screened ligand-receptor (LR) pairs of neural cell types specific to ECs. Meanwhile, we also added the Wnt7 family-related LR pairs that were reported to be essential for early CNS vascularization in mice,^{2,3} but these interactions were relatively weak during human brain BBB development. Notably, we detected a strong CDH2-CDH2 interaction between neural cells and ECs, and such an interaction was reported to be involved in the regulation of β -catenin (Figures 3C, S4C, and S4D; Table S4).^{37,38} From GW6 to GW21, NPCs and

Figure 2. The changes in the expression of BBB-related genes in EC subclusters during BBB development

- Violin plot showing expression of BBB-related transporter-related genes in each EC subcluster from embryonic/fetal to adult stage.
- Boxplot displaying the score of expression of transporter-related genes in EC subclusters from GW5 to adult, including our data (red box), data from Zeng et al.³⁰ (green box), and data from Wälchli et al.⁷ (blue box).
- Spatial visualization of representative transporter-related gene expression of transcripts using MERFISH in ECs at GW6–GW16.
- Spatial visualization of expression score of transporter-related genes in ECs at GW6–GW16 using MERFISH. These enlarged boxes label more detailed subregions.
- Representative immunofluorescence staining for CD31 and MFSD2A in human brain at GW6 and cerebral cortices at GW7–GW21. For adult stage, CD31, MFSD2A, and SLC16A1 antibodies were used for immunostaining in human cerebral cortex.
- Line chart showing normalized intensity of MFSD2A in CD31⁺ cells at GW6–GW21 and normalized intensity of MFSD2A in SLC16A1⁺CD31⁺ cells at the adult stage.
- Representative immunofluorescence staining for CD31, MFSD2A, and GJA5 in human cerebral cortex at the adult stage.
- Representative immunofluorescence staining for CD31 and SLC1A4 in human brain at GW6 and cerebral cortices at GW7–GW21 and adult stage.
- Line chart displaying normalized intensity of SLC1A4 in CD31⁺ cells.

In (F) and (I), $n = 6$ independent repeated experiments. Bars represent mean \pm SEM. Unpaired two-tailed t test: n.s., not significant, * $p < 0.05$, ** $p < 0.01$, *** $p < 0.001$. In (B) and (D), the transporter-related genes (Table S5) were used to calculate module scores by AddModuleScore function from Seurat. For detailed procedures, please refer to the “BBB scores” description in the STAR Methods. Adu, adult; CP, cortical plate; IZ, intermediate zone; VZ, ventricular zone; SVZ, subventricular zone. See also Figure S3 and Table S5.

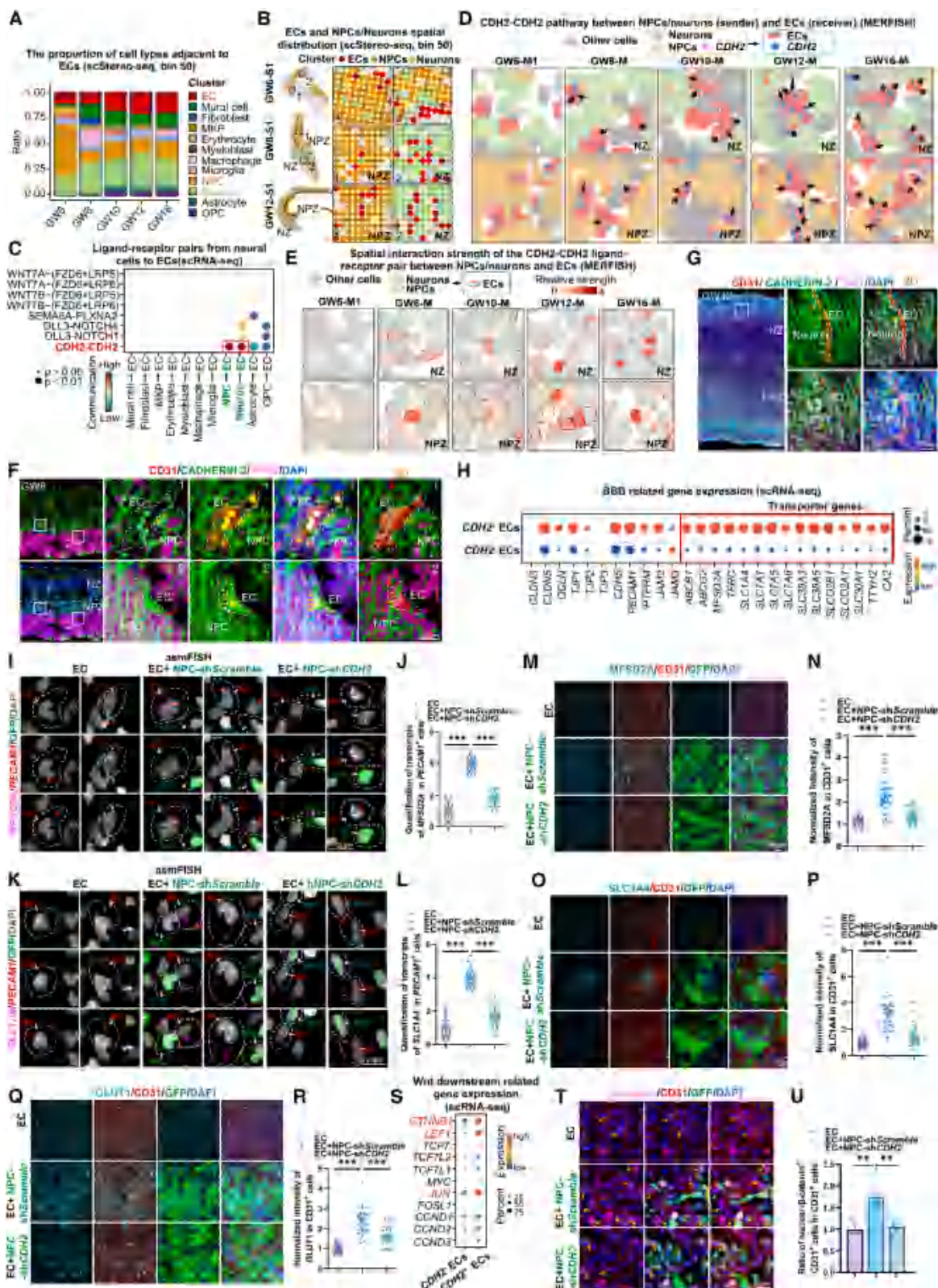


Figure 3. Neural cells contribute to BBB-specific transporter expression

(A) Bar plots showing ratios of cell types adjacent to ECs in different stages based on scStereo-seq.

(B) Spatial visualization of ECs, NPCs, and neurons in different stages.

(legend continued on next page)

neurons accounted for the main contribution to the CDH2-CDH2 pathway (Figure S4E). The spatial transcriptomics results demonstrated that, at GW6, both the NPCs/neurons and ECs exhibited weak CDH2-CDH2 signals. However, starting from GW8, both the NZ and NPZ regions displayed strong signals (Figure 3D). We further calculated the spatial interaction strength of CDH2-CDH2 between NPCs/neurons and ECs using CMMOT.³⁵ The results also revealed weak spatial interaction strength at GW6 that markedly intensified from GW8 in both cortical zones (Figure 3E). Immunofluorescence staining experiments were performed to further confirm these results (Figures 3F, 3G, and S4F).

First, we divided the ECs into CDH2-positive and CDH2-negative groups. Compared with CDH2-negative ECs, CDH2-positive ECs exhibited stronger BBB properties (Figure 3H). Moreover, genes downstream of the β -catenin pathway associated with the BBB (i.e., *CTNFB1*, *LEF1*, and *JUN*)¹⁵ were also significantly activated in CDH2-positive ECs (Figure 3S). Next, we validated these results using *in vitro* co-culture experiments, in which human embryonic stem cell (hESC)-derived differentiated NPCs or neurons were co-cultured with a human brain EC cell line. Using immunofluorescence staining, we observed that CDH2 signals are detectable at EC-NPC/neuron junctions in the co-culture system (Figure S4G). Next, amplification-based single-molecule fluorescence *in situ* hybridization (asmFISH) experiments were performed to validate transcriptomic-level alterations of BBB-related transporter genes. Compared with ECs in the non-co-culture groups, co-cultured ECs significantly upregulated BBB-specific transporter-related genes (i.e., *MFSD2A* and *SLC1A4*), and this upregulation was abolished by CDH2 knockdown (KD) in neural cells (Figures 3I–3L and S5C–S5F). We also verified the KD efficiency of CDH2 in neural cells through western blotting (Figures S5A and S5B). Meanwhile, immunofluorescence

staining experiments revealed that, compared with the control groups, expression levels of BBB-related transporter proteins (i.e., *MFSD2A*, *SLC1A4*, *GLUT1*, and *ABCG2*) were significantly increased in the co-culture groups, whereas CDH2 KD groups exhibited markedly decreased protein expression levels (Figures 3M–3R and S5G–S5L). To assess whether the β -catenin signaling pathway is specifically activated, nuclear β -catenin was analyzed by immunofluorescence staining. Compared with control groups, the co-culture groups displayed a significant accumulation of nuclear- β -catenin, whereas the CDH2 KD groups showed diminished nuclear localization (Figures 3T, 3U, S5M, and S5N). Similarly, the β -catenin downstream-activated transcription factor JUN showed congruent results (Figures S5O and S5P). Therefore, the results suggest that neural cells can specifically activate the β -catenin signaling pathway via upstream CADHERIN-2 (CDH2) signaling, which further promotes the expression of BBB-specific transporter genes in ECs.

NPCs promote mural cell proliferation

Mural cells are necessary for BBB formation and essential for BBB integrity.³⁹ To delineate the mural cell heterogeneity, we identified five distinct subclusters (Figures 4A and S6A–S6E). Surprisingly, we found that proliferating mural cells were mainly distributed in the NPZ (Figures 4B, 4C, and S6F–S6I), which was corroborated by immunofluorescence staining (Figures 4D, 4E, S6J, and S6K). This spatial correlation suggested that NPCs may affect the proliferation of mural cells. By analyzing scRNA-seq data, we identified NPC-mural-cell-specific PDGFD-PDGFRB LR pair (Figure 4F; Table S4). It has been reported that PDGFD can promote the proliferation of PDGFRB-positive cells.^{40,41} Using spatial data, we found that PDGFD was mainly expressed in NPCs within NPZ

(C) Dot plot showing the specific pathways of neural cells toward ECs and the Wnt7 pathways.

(D) Spatial visualization of CDH2-CDH2 pathway between NPCs/neurons and ECs using MERFISH. The pink and blue dots represent the expression of CDH2 transcripts in NPCs/neurons and ECs, respectively.

(E) Spatial visualization of interaction strength of the CDH2-CDH2 LR pair between NPCs/neurons and ECs using MERFISH. For detailed procedures, please refer to the “COMMOT”³⁵ description in the STAR Methods.

(F) Representative immunofluorescence images for CD31, CDH2, and SOX2 in GW8 human cerebral cortex. The yellow arrows show the boundary of the interaction between SOX2⁺CDH2⁺ NPCs and CD31⁺CDH2⁺ ECs.

(G) Representative immunofluorescence images for CD31, CDH2, and TUJ1 in GW12 human cerebral cortex. The yellow arrow shows the boundary of the interaction between TUJ1⁺CDH2⁺ neurons and CD31⁺CDH2⁺ ECs.

(H) The dot plot showing the expression of BBB-related genes in CDH2-negative and CDH2-positive ECs.

(I) asmFISH of MFSD2A and PECAM1 in human-brain-derived ECs or ECs and ES-derived NPCs of co-culture.

(J) Quantification of transcripts of MFSD2A in PECAM1⁺ cells.

(K) asmFISH of SLC1A4 and PECAM1 in human-brain-derived ECs or ECs and ES-derived NPCs of co-culture.

(L) Quantification of transcripts of SLC1A4 in PECAM1⁺ cells.

(M) Immunostaining for MFSD2A and CD31 in human-brain-derived ECs or ECs and ES-derived NPCs of co-culture.

(N) Quantification of the normalized intensity of MFSD2A on the surface of CD31⁺ cells.

(O) Immunostaining for SLC1A4 and CD31 in human-brain-derived ECs or ECs and ES-derived NPCs of co-culture.

(P) Quantification of the normalized intensity of SLC1A4 in the surface of CD31⁺ cells.

(Q) Immunostaining for GLUT1 and CD31 in human-brain-derived ECs or ECs and ES-derived NPCs of co-culture.

(R) Quantification of the normalized intensity of GLUT1 on the surface of CD31⁺ cells.

(S) The dot plot showing the expression of Wnt downstream-related genes in CDH2⁻ and CDH2⁺ ECs.

(T) Immunostaining for β -catenin and CD31 in human-brain-derived ECs or ECs and ES-derived NPCs of co-culture. Arrowheads indicating nuclear- β -catenin⁺CD31⁺ cells.

(U) Ratio of nuclear- β -catenin⁺CD31⁺ cells in CD31⁺ cells.

In (J) and (L), each point represents quantification of transcripts in PECAM1⁺ cells. 30 cells were counted in 6 independent repeated experiments. In (N), (P), and (R), each point represents the normalized fluorescence density of one cell. 30 cells were counted in 6 independent repeated experiments. In (U), $n = 6$ independent repeated experiments. Bars represent mean \pm SEM. Unpaired two-tailed t test: ** $p < 0.01$, *** $p < 0.001$. NPZ, NPC-enriched zone; NZ, neuron-enriched zone. See also Figures S4 and S5 and Tables S4 and S7.

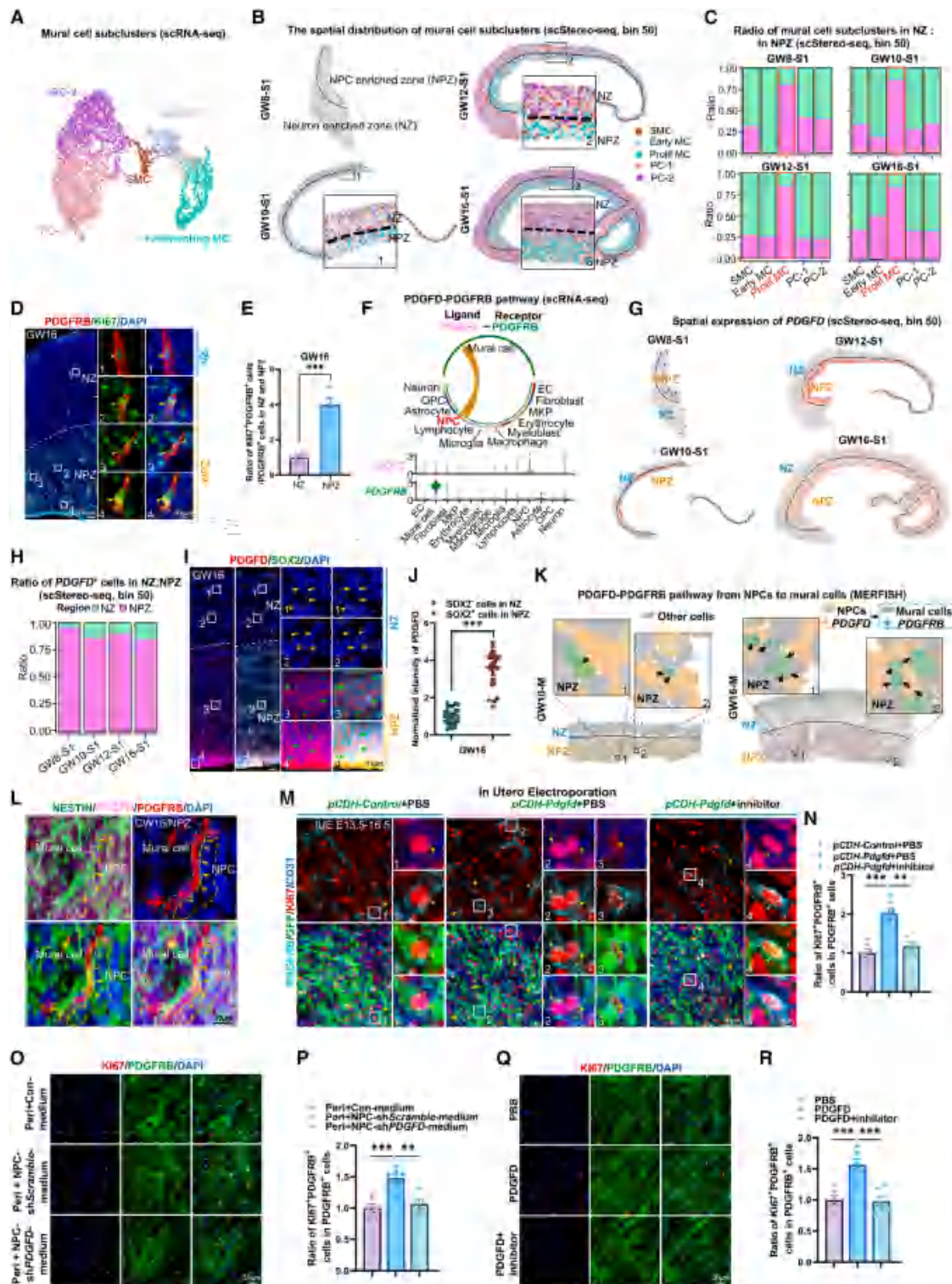


Figure 4. NPCs promote the proliferation of mural cells

(A) UMAP visualization showing the re-clustered mural cell subclusters.

(B) Spatial visualization of mural cell subclusters in NPZ and NZ of GW8–GW16 cerebral cortices.

(legend continued on next page)

(Figures 4G, 4H, S6L, and S6M). Immunofluorescence staining confirmed this result (Figures 4I and 4J). Moreover, through spatial transcriptomics and immunofluorescence, we demonstrated the specific ligand (PDGFD)-receptor (PDGFRB) expression between NPCs and mural cells (Figures 4K and 4L).

To determine whether the PDGFD-PDGFRB pathway could promote mural cell proliferation, we conducted a series of *in vivo* and *in vitro* experiments to validate its role. First, we performed *in utero* electroporation experiments, and the results showed that overexpression of PDGFD in NPCs resulted in enhanced proliferation of mural cells in the NPZ, while concurrent PDGFRB blockade abolished this effect (Figures 4M and 4N). Next, *in vitro*, we found that adding the supernatant of NPCs promoted the proliferation of pericytes, whereas using the supernatant of NPCs with PDGFD KD weakened proliferation (Figures 4O and 4P). Finally, we performed pericyte proliferation assays with PDGFD protein and PDGFRB inhibitor treatment and found that, compared with the control group, adding PDGFD protein significantly promoted pericyte proliferation, whereas the further addition of the PDGFRB inhibitor markedly suppressed this effect. This result indicated that PDGFD could promote pericyte proliferation through the PDGFRB receptor pathway *in vitro* (Figures 4Q and 4R). Consistently, the ELISA assay demonstrated that NPCs secreted PDGFD protein, and PDGFD KD significantly reduced PDGFD protein levels in the supernatant (Figure S6N). Overall, we proved that NPCs could secrete PDGFD to promote the proliferation of mural cells through a series of functional experiments *in vitro* and *in vivo*.

The crosstalk between ECs and mural cells

The signaling communication between ECs and mural cells is crucial for the maturation of the BBB.^{21,39,42} ECs play a critical role in recruiting mural cells through a series of signals.^{43,44} We detected that the speculated interactions of classic recruitment signaling pathways (e.g., PDGFB-PDGFRB, Delta-like ligand [DLL]4-NOTCH3, and JAG1-NOTCH3)^{39,45–47} from ECs to mural

cells began to strengthen at GW8 (Figures 5A and S7B–S7D). These findings were corroborated by MERFISH (Figures 5B, 5C, and S7E) and immunofluorescence staining (Figure 5D). Notably, we found that, from GW8, the expression of recruitment-related LR pairs between ECs and mural cells in the NZ region was higher than that in the NPZ region (Figures 5B, 5C, and S7E).

Interestingly, we revealed that ECs in the NZ had higher scores for TJ-related genes and BBB-specific transporter-related genes (Figures 5E–5H). As development progressed, proliferating ECs exhibited a higher localization preference in the NPZ region, while other EC subclusters predominantly occupied the NZ region (Figure S7F). Furthermore, the NZ region contained a higher proportion of mature mural cell subclusters (e.g., PC-1 and PC-2) within the perivascular compartment compared with the NPZ region. In contrast, proliferating mural cells showed obviously enriched perivascular localization in NPZ (Figures 5I and S7G).

Meanwhile, we found that, from GW8 onward, the speculative interaction strength of the PDGFB-PDGFRB between ECs and mural cells progressively increased during development, with stronger interactions in the NZ than in the NPZ (Figure 5J). These results suggested that neurons might affect the distribution of these subclusters. Thus, we investigated the signaling pathways underlying the recruitment of mural cells by neurons and detected higher expression levels of DLL3 in neurons than in ECs (Figures S7A and S7B). As previously reported, DLL3 is an inhibitory ligand in the Notch signaling pathway^{48–50}; however, its potential involvement in mural cell recruitment remains to be further investigated.

Next, we analyzed the signaling interactions between mural cells and ECs (Figures S7C and S7D). Notably, mural cells could secrete a range of signals associated with the maturation of the BBB in ECs,¹ including TGF β signaling (Figures 5K and S7H),⁵¹ ANGPT2-TEK signaling (Figure 5L),^{52,53} and extracellular matrix (ECM)-related signaling (i.e., collagen, laminin, and fibronectin) (Figures S7I–S7L).⁵⁴ More importantly, spatial transcriptomic

(C) Bar plots showing the ratio of mural cell subclusters in NZ: in NPZ of GW8–GW16 cerebral cortices.

(D) Representative immunofluorescence images for PDGFRB and Ki67 in cerebral cortex at GW16.

(E) Bar graph showing the ratio of Ki67⁺PDGFRB⁺ cells in NPZ and NZ of GW16 cerebral cortex.

(F) Upper, chord plot showing pathway of PDGFD-PDGFRB between other major cell types and mural cell at GW16 using Cell Chat; lower, violin plot showing the expression of *PDGFD* and *PDGFRB* in other major cell types and mural cell.

(G) Spatial visualization of expression of *PDGFD* in cerebral cortices of GW8–GW16.

(H) Bar plot showing the ratio of *PDGFD*⁺ cells in NZ: in NPZ of GW8–GW16 cerebral cortices.

(I) Representative immunofluorescence images for PDGFD and SOX2 in cerebral cortex at GW16.

(J) Quantification of the normalized intensity of PDGFD in SOX2⁻ cells in NZ and SOX2⁺ cells in NPZ.

(K) Spatial visualization of PDGFD-PDGFRB pathway between NPCs and mural cells using MERFISH. The pink dots represent the expression of *PDGFD* transcripts in NPCs, and blue dots represent the expression of *PDGFRB* transcripts in mural cells.

(L) Representative immunofluorescence images for NESTIN, PDGFD, and PDGFRB in GW16 NPZ of human cerebral cortex. The yellow arrows show the boundary of the interaction between NESTIN⁺PDGFD⁺ NPCs and PDGFRB⁺ mural cells.

(M) Control plasmids with PBS, *Pdgfd* overexpression plasmids with PBS, and *Pdgfd* overexpression plasmids with a PDGFRB inhibitor were electroporated into E13.5 embryonic mouse brains, respectively, and the brains were harvested at E16.5 for anti-PDGFRB, Ki67, and CD31 immunostaining.

(N) Quantification of ratio of Ki67⁺PDGFRB⁺ cells in PDGFRB⁺ cells.

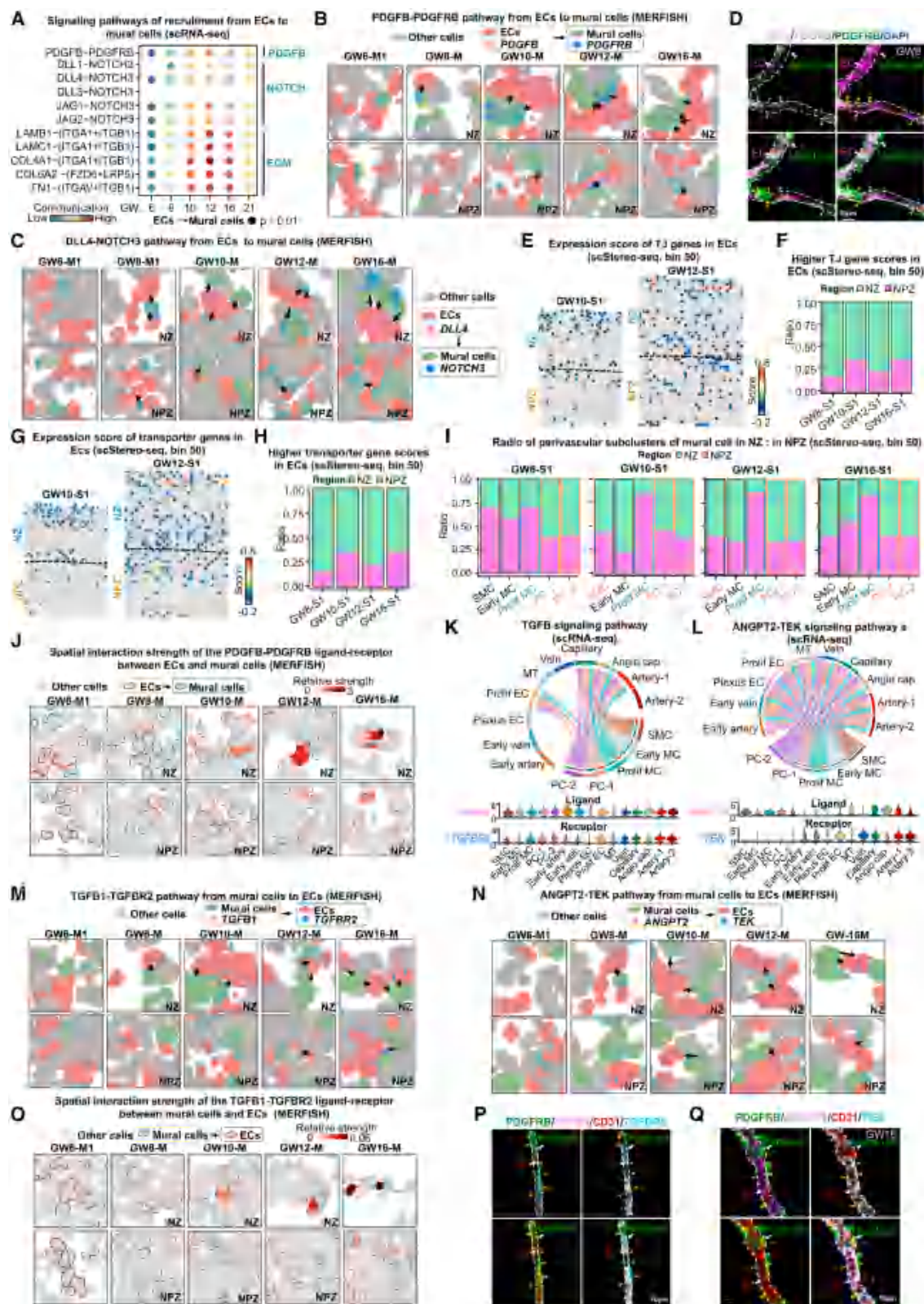
(O) Immunostaining for Ki67 and PDGFRB in human-brain-derived pericytes with distinct medium.

(P) Quantification of ratio of Ki67⁺PDGFRB⁺ cells in PDGFRB⁺ cells.

(Q) Human brain-derived pericytes were subjected to immunofluorescence staining for Ki67 and PDGFRB following treatment with PBS, PDGFD, or PDGFD combined with a PDGFRB inhibitor.

(R) Quantification of ratio of Ki67⁺PDGFRB⁺ cells in PDGFRB⁺ cells.

In (E), $n = 5$ independent repeated experiments. In (J), each point represents the normalized fluorescence density of one cell. 30 cells were counted in 6 independent repeated experiments. In (N), (P), and (R), $n = 6$ independent repeated experiments. Bars represent mean \pm SEM. Unpaired two-tailed t test: ** $p < 0.01$, *** $p < 0.001$. MC, mural cell; PC, pericyte. See also Figure S6 and Tables S2, S3, S4, and S7.



(legend on next page)

analyses confirmed progressive pathway activation during BBB ontogeny (Figures 5M–5O). Finally, immunofluorescence staining validated these LR expressions between mural cells and ECs (Figures 5P, 5Q, and S7M). Collectively, these findings demonstrate that enhanced EC-mural cell crosstalk initiates at GW8 and exhibits spatial heterogeneity, with stronger intercellular communication in the NZ versus the NPZ.

BBB development is relatively conserved between humans and mice

According to the corresponding periods of human and mouse development in a previous study (Figure 6A),⁵⁵ we used FACS to enrich mouse CD31-positive cells from heads at embryonic day 10.5 (E10.5) and cerebral cortices at E13.5 to postnatal day 20 (P20) for scRNA-seq. After quality control (Figure S8A; Table S1) and clustering (Figures S8B and S8C), 39,635 mouse ECs were subjected to subsequent comparative analysis. Based on the expression patterns of classical marker genes,^{15,16} mouse ECs were classified into ten subclusters (Figures S8D and S8E; Table S2). It is interesting to note that during the integration process of human and mouse EC subclusters, at P20, the two mouse subclusters—mCapillary-A and mArtery ECs—failed to mix well with human ECs, potentially attributable to the absence of age-matched human samples (Figures 6B and S8F).

We also analyzed the developmental trajectory of mouse EC subclusters. Analysis revealed overall similarities to that of human ECs (Figures S8G–S8I). Furthermore, we compared the developmental trajectories between human and mouse ECs.⁵⁶ The results demonstrated that human ECs differentiate from capillary ECs into artery-1 ECs and subsequently into artery-2 ECs, whereas mouse ECs progress from mCapillary-A ECs to mArtery ECs (Figures 6C–6E).

Pearson correlation analysis of BBB-related genes (Table S5) demonstrated strong human-mouse correspondence between

GW8–GW21 and E13.5–P2 ECs (Figure 6F). Next, we analyzed the expression of representative BBB-related genes in human and mouse ECs across different developmental stages, where human adult data⁷ and P60 mouse data¹⁶ were obtained from the published studies. These datasets revealed conserved developmental regulation (Figure 6G). In addition, the expression pattern of transporter-related genes in EC subclusters is also consistent between humans and mice (Figures 2A and S8J).

We next compared the correlation of BBB-related genes between human and mouse EC subclusters and detected a high similarity during development (Figure S8K). Moreover, we performed a differential expression analysis of BBB-related genes between human and mouse ECs. Intriguingly, we identified the differentially expressed genes between humans and mice (Figure 6H). Immunofluorescence validation confirmed the high expression of INSR⁵⁷ in human ECs of the cerebral cortex (Figures 6I and 6J). Taken together, these results show that BBB development is generally conserved between humans and mice.

Deletion of H2A.Z.1 in ECs affects angiogenesis and disrupts BBB development

Notably, the comparison between human and mouse ECs identified a key gene, *H2AFZ* (*H2afz*), encoding H2A.Z.1, which was highly expressed in the early developmental stages of human and mouse EC subclusters (i.e., early ECs, plexus ECs, and proliferating ECs) (Figure 7A). Immunofluorescence staining further confirmed robust H2A.Z.1 expression in cortical ECs of both species (Figures 7B and 7C). In addition, it has been reported that H2A.Z.1 is involved in regulating the Wnt signaling pathway downstream.⁵⁸ Given the importance of the Wnt signaling pathway for CNS vascularization,^{2,3} we hypothesized a potential regulatory function for H2A.Z.1 in early BBB development.

Figure 5. The crosstalk between ECs and mural cells

- (A) Dot plot showing signaling pathways of recruitment from ECs to mural cells.
- (B) Spatial visualization of the PDGFB-PDGFRB pathway between ECs and mural cells at GW6–GW16 using MERFISH. The pink dots represent the expression of *PDGFB* transcripts in ECs, and the blue dots represent the expression of *PDGFRB* transcripts in mural cells.
- (C) Spatial visualization of DLL4-NOTCH3 pathway between ECs and mural cells at GW6–GW16 using MERFISH. The pink dots represent the expression of *DLL4* transcripts in ECs, and the blue dots represent the expression of *NOTCH3* transcripts in mural cells.
- (D) Immunostaining for CD31, PDGFB, and PDGFRB in cerebral cortex at GW8.
- (E) Spatial visualization of the scores of TJ genes in NPZ and NZ in cerebral cortices of GW10 and GW12.
- (F) The bar charts showing the proportion of EC with TJ gene scores greater than -0.1 in NPZ and NZ in cerebral cortices of GW8–GW16.
- (G) Spatial visualization of transporter-related gene scores in NPZ and NZ in cerebral cortices of GW10 and GW12.
- (H) The bar charts showing the proportion of EC with transporter-related gene scores greater than -0.1 in NPZ and NZ in cerebral cortices of GW8–GW16.
- (I) Ratio of perivascular subclusters of mural cells in NZ: in NPZ at GW8–GW16.
- (J) Spatial visualization of interaction strength of the PDGFB-PDGFRB LR pair between ECs and mural cells using MERFISH.
- (K) Upper, chord plot showing TGFB signaling pathway between mural cell subclusters (ligand) and EC subclusters (receptor) using Cell Chat; lower, violin plot showing the expression of *TGFB1* and *TGFB2* in mural cell and EC subclusters.
- (L) Upper, chord plot showing ANGPT2-TEK signaling pathway between mural cell subclusters (ligand) and EC subclusters (receptor) using Cell Chat; lower, violin plot showing the expression of *ANGPT2* and *TEK* in mural cell and EC subclusters.
- (M) Spatial visualization of TGFB1-TGFB2 pathway between mural cells and ECs at GW6–GW16 using MERFISH. The pink dots represent the expression of *TGFB1* transcripts in mural cells, and the blue dots represent the expression of *TGFB2* transcripts in ECs.
- (N) Spatial visualization of ANGPT2-TEK pathway between mural cells and ECs at GW6–GW16 using MERFISH. The pink dots represent the expression of *ANGPT2* transcripts in mural cells, and the blue dots represent the expression of *TEK* transcripts in ECs.
- (O) Spatial visualization of interaction strength of the TGFB1-TGFB2 LR pair between mural cells and ECs using MERFISH.
- (P) Representative immunofluorescence images for PDGFRB, TGFB1, CD31, and TGFB2 in GW16 human cerebral cortex. The yellow arrows show the boundary of the interaction between PDGFRB⁺TGFB1⁺ mural cells and CD31⁺TGFB2⁺ ECs.
- (Q) Representative immunofluorescence images for PDGFRB, ANGPT2, CD31, and TIE2 in GW16 human cerebral cortex. The yellow arrows show the boundary of the interaction between PDGFRB⁺ANGPT2⁺ mural cells and CD31⁺TIE2⁺ ECs.

See also Figure S7 and Tables S4 and S5.

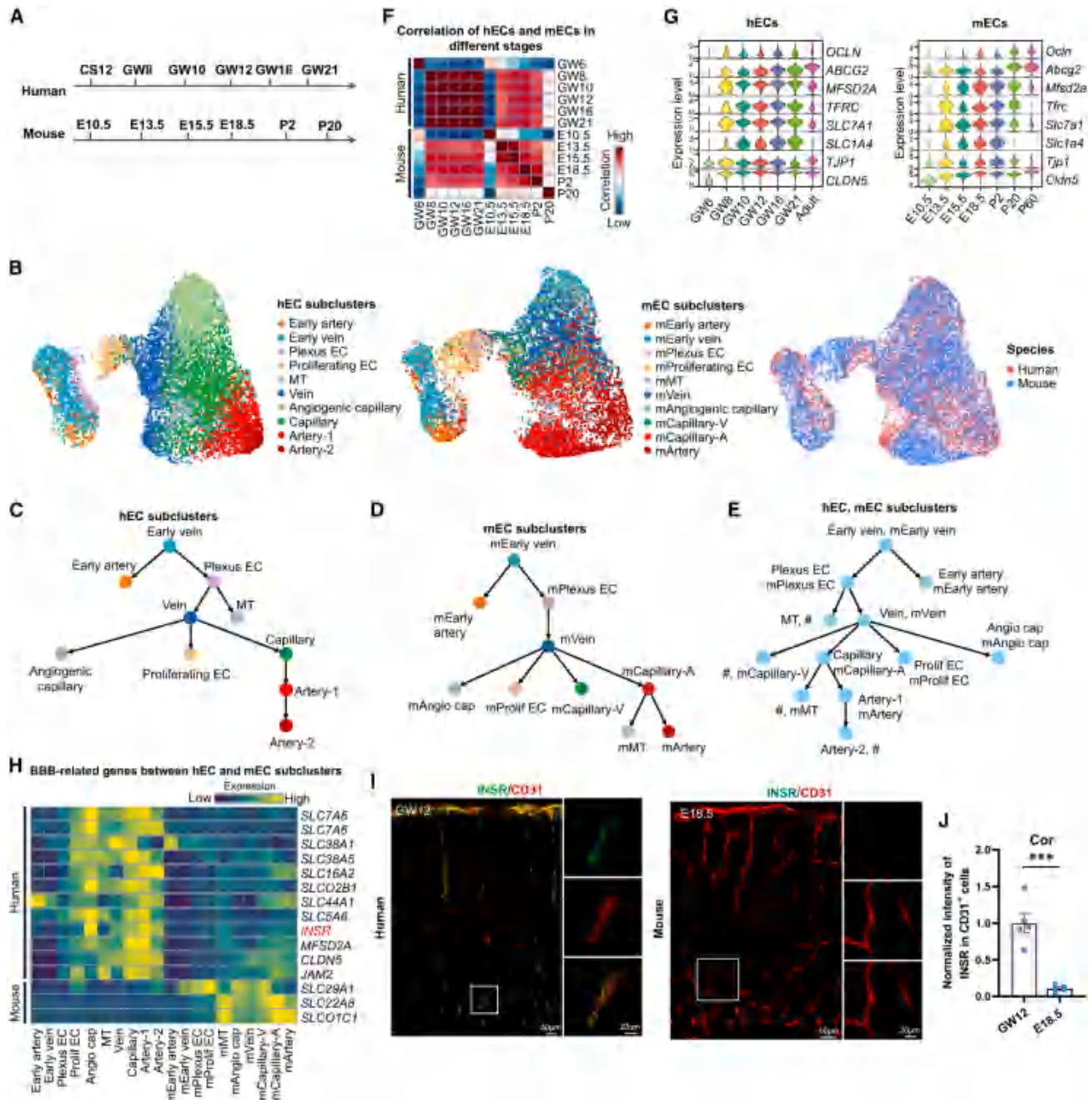


Figure 6. BBB development of ECs is approximately conserved in humans and mice

(A) Overview of the developmental stages for comparison between human and mouse.

(B) Visualization of hEC and mEC subclusters (to show the cell types more clearly, 12,030 hECs and 11,820 randomly selected mECs were used for 2D display) using Seurat.

(C) A trajectory tree of hEC subclusters predicted by CAPITAL. Nodes in the trajectory tree correspond to clusters consistent with those in Figure 1E.

(D) A trajectory tree of mEC subclusters predicted by CAPITAL. Nodes in the trajectory tree correspond to clusters consistent with those in Figure S8D.

(E) An aligned tree of the trajectories of clusters, where each pair of clusters in a node denotes the clusters shown in (C) and (D).

(F) Correlation of different stages of BBB development in human and mouse ECs.

(G) Violin plots showing expression of representative BBB-related genes in human and mouse ECs. Data on human adult ECs were derived from this published study,⁷ while data for mouse ECs at P60 were obtained from another study.¹⁶

(H) Heatmap showing representative DEGs expression of BBB between hEC and mEC subclusters.

(legend continued on next page)

To investigate H2A.Z.1's role in BBB development, we constructed endothelial-specific *H2afz* knockout (KO) mice (Figure S9A). We found that conditional *H2afz* KO in ECs disrupted cerebral cortical angiogenesis (Figures S9B–S9F). Moreover, we detected BBB-related indicators and found that leakage increased after *H2afz* KO in ECs at E15.5 (Figures 7D, 7E, S9G, and S9H). To explore the reasons, we first performed immunofluorescence staining assays and detected no evident change in the TJ-related protein CLAUDIN5 upon *H2afz* KO in ECs at E15.5 (Figures S9K and S9L). In contrast, the transporter-related proteins MFSD2A¹⁴ and GLUT1 decreased significantly (Figures 7F–7I). Simultaneously, we assessed transcytosis in ECs by immunofluorescence staining for caveolin-1 (CAV-1), which was significantly upregulated following *H2afz* KO, suggesting enhanced transcytosis as a driver of vascular leakage (Figures S9I and S9J). Furthermore, we isolated cerebrovascular ECs and analyzed the expression of MFSD2A, GLUT1, and CAV-1 proteins after *H2afz* KO in ECs via western blot (Figures 7J and 7K). The results were concordant with the immunofluorescence staining data.

Moreover, we further utilized transmission electron microscopy (TEM) to examine the impact of *H2afz* endothelial KO on the BBB. To evaluate whether *H2afz* affects endothelial transcytosis, we employed TEM to visualize transcytotic vesicles in cerebrovascular endothelia following *H2afz* KO in ECs at E17.5. For quantification, trans-endothelial vesicles were classified into three categories: type 1 vesicles are those luminal membrane-connected, type 2 vesicles are fully formed vesicles undergoing cytoplasmic transport, and type 3 vesicles are abluminal membrane connected. Compared with the control group, all three types of transcytotic vesicles were significantly increased in cerebrovascular endothelia of *H2afz* conditional KO mice (Figures 7L and 7M). Additionally, TEM observations revealed no ultrastructural abnormalities in the TJs of brain ECs (continuous electron-dense linear structures) (Figure S9M).

Previous studies have reported the involvement of *H2afz* in cellular proliferation.^{59,60} In this study, we also observed that *H2afz* endothelial-specific KO in E15.5 mice significantly attenuated the proliferation in both cerebral cortex and peripheral organ ECs (Figures S9N–S9Q). These results suggest that the conditional KO of *H2afz* in ECs may broadly disrupt EC homeostasis, thereby disrupting BBB development. Meanwhile, we observed that, at P2 and P7, *H2afz* endothelial-specific mice exhibited sustained leakage (Figures S9R–S9U). Immunofluorescence staining revealed that, at P7, the protein expression levels of the transporters MFSD2A and GLUT1 in ECs were significantly reduced following *H2afz* KO in ECs (Figures S10A–S10D), whereas CAV-1 expression was increased (Figures S10E and S10F). Next, we examined endothelial TJ function and transcytosis in P14 mice following horseradish peroxidase (HRP) injection. Using TEM, we observed that, in both the control and *H2afz* endothelial-specific KO groups, HRP was halted at the TJs, creating a distinct boundary between HRP-positive and HRP-negative regions, with no leakage through the TJs detected

(Figure S10G). Furthermore, we revealed that endothelial-specific KO of *H2afz* resulted in a significant increase in HRP-positive vesicle numbers compared with the control group, demonstrating enhanced transcytosis activity (Figures S10H and S10I). These results indicate that conditional KO of *H2afz* in ECs continues to affect postnatal vascular homeostasis and impairs BBB development. Given that the endothelial-specific KO of *H2afz* impacted the expression of BBB-related transporters, we further investigated potential alterations in blood-to-brain metabolic transport using CY3-labeled glutamine (Gln)^{61–63} and found that, upon KO of *H2afz* in ECs, the intensity of Gln-Cy3 in the brain significantly decreased (Figures 7N and 7O).

β -catenin is essential for BBB development³ and for the regulation of BBB-related transporters.^{2,3,64} Therefore, we speculated whether H2A.Z.1 could affect the β -catenin signaling pathway.⁵⁸ First, immunofluorescence staining revealed that β -catenin-specifically activated effectors, including nuclear- β -catenin, TCF1, and LEF1, were significantly reduced in ECs following *H2afz* endothelial-specific KO (Figures 7P, 7Q, and S10J–S10M). Concurrently, western blot analysis demonstrated that the expression levels of Wnt downstream-activated signaling proteins, TCF1 and LEF1, were also markedly decreased (Figures 7R and 7S). H2A.Z.1 can regulate downstream gene expression by recruiting certain proteins.⁶⁵ Therefore, we performed experiments to verify whether H2A.Z.1 interacts with β -catenin. Co-immunoprecipitation experiments revealed that H2A.Z.1 could indeed interact with β -catenin (Figures 7T–7W). In addition, using chromatin immunoprecipitation (ChIP) experiments, we revealed that both H2A.Z.1 and β -catenin could bind to the promoter region of *Mfsd2a* to regulate its expression (Figures S10N and S10O). After *H2afz* KD in ECs, the binding of β -catenin to the promoter region of *Mfsd2a* weakened, whereas after overexpressing *H2afz*, the binding strengthened (Figures S10P and S10Q). However, *Ctnnb1* (encoding β -catenin) KD had no significant effect on the binding of H2A.Z.1 to the promoter region of *Mfsd2a* (Figure S10R). In summary, our study demonstrates that the conditional KO of *H2afz* in ECs impairs EC homeostasis, and this imbalance subsequently disrupts angiogenesis and BBB development.

DISCUSSION

As the BBB is crucial for normal development of the brain,^{66,67} it is vital to explore the mechanisms regulating BBB formation. Previous studies in mice mainly focus on certain molecules in specific cell types.^{2,3,68–70} In studies of developing human brain vascular research, only brain ECs and mural cells have been examined.^{7,21} However, the initiation and establishment of the BBB in the human brain remain unclear. In this work, we established a spatiotemporal developmental atlas of the human BBB and explored the molecular mechanisms underlying BBB initiation and development.

We identified the initiation of a BBB-like transcriptional signature in humans at GW8. Previous investigations have utilized

(I) Representative immunofluorescence images for INSR and CD31 in GW12 human and E18.5 mouse cerebral cortex.

(J) Normalized intensity of INSR in CD31⁺ cells in GW12 human and E18.5 mouse cerebral cortices.

In (J), $n = 5$ independent repeated experiments. Unpaired two-tailed t test: *** $p < 0.001$.

h, human; m, mouse. See also Figure S8 and Tables S1, S2, and S5.

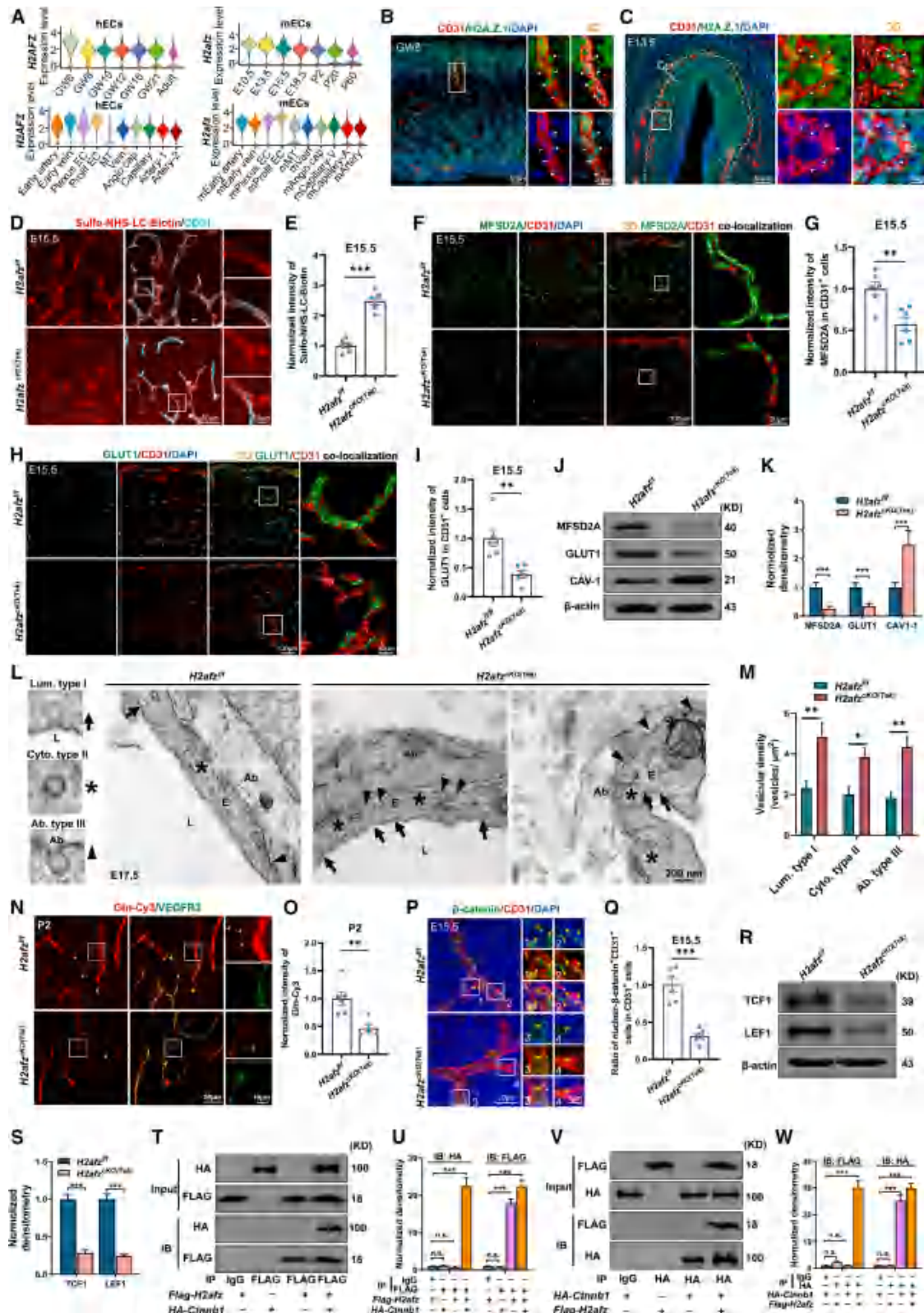


Figure 7. H2A.Z.1 regulates BBB development

(A) Violin plots showing expression trends of *H2AFZ*/*H2afz* in hECs and mECs. Data of human adult ECs were derived from this published study,⁷ and data for mouse ECs at P60 were obtained from another study.¹⁶

(legend continued on next page)

immunostaining to examine the expression of certain BBB-related markers at specific time points,^{71,72} but it is impossible to systematically investigate the precise changes in the molecular characteristics of ECs during BBB development. Single-cell spatiotemporal transcriptome analysis revealed that vascularization of the human brain commenced at GW6, but ECs do not exhibit BBB-like properties at this stage. Interestingly, we found that most transporter-related genes were ubiquitously expressed in embryonic and fetal EC subclusters, whereas in adulthood, their expression became more specialized.

It has been reported that ligands secreted by NPCs, such as VEGF⁷³ and Wnt,^{2,3,69} are essential for the initial vascularization of the CNS. In this study, we newly identified a non-Wnt signal, CADHERIN-2 (*CDH2*), expressed by neural cells, which was found to activate the β -catenin signaling pathway^{37,38} and subsequently induce the expression of BBB-specific transporters in ECs. These findings broaden our understanding of neural-cell-mediated induction of BBB development in ECs.

Moreover, we have revealed the regulatory roles of NPCs in mural cell development. We found that NPCs could promote the proliferation of mural cells through the secretion of PDGFD.^{41,74,75} Previous studies have reported that PDGFB KO exhibits a phenocopy of PDGFRB KO, i.e., the absence of mural cells in the brain parenchyma.^{39,76,77} However, our finding that PDGFD secreted by NPCs can promote mural cell proliferation is not contradictory to previous research, as mural cells also require additional factors to regulate their subsequent development after their formation in the brain.

More importantly, we discovered that, following initiation of the BBB-like transcriptomic signature (GW8), signaling crosstalk be-

tween ECs and mural cells strengthened. Compared with the NPZ, the NZ showed higher EC-mural cell signaling interactions and greater BBB maturity. In addition, we revealed that the specialization patterns of vascular development and BBB development are generally conserved between humans and mice and identified a critical molecule, H2A.Z.1. Through a series of *in vivo* validation experiments, we demonstrated that conditional KO of *H2afz* in ECs broadly impairs endothelial homeostasis, and these imbalances subsequently disrupt angiogenesis and BBB development.

In summary, our study provides insights into the regulation of BBB development through NVU-related cell interactions, which may provide potential targets and conceptual frameworks for the treatment of BBB-related diseases (Figure S10S).

Limitations of the study

First, owing to the high dropout rate of the spatial transcriptome, the integration method between scRNA-seq and spatial transcriptomics needs to be improved. Second, as transporter-related genes are generally expressed in developmental ECs but gradually specialize in adulthood, the underlying mechanism needs to be further investigated. Third, due to current limitations in sequencing technologies, even scRNA-seq cannot capture many low-abundance genes (e.g., numerous receptor genes), which may result in missing critical LR interaction pairs.

RESOURCE AVAILABILITY

Lead contact

Further queries and reagent requests may be directed to and will be fulfilled by the lead contact, Jianwei Jiao (jwjiao@ioz.ac.cn).

- (B) Representative immunofluorescence images for CD31 and H2A.Z.1 in human cerebral cortex at GW8. Imapris 3D reconstruction showing the expression of CD31 and H2A.Z.1.
- (C) Representative immunofluorescence images for CD31 and H2A.Z.1 in mouse cerebral cortex at E13.5. Imapris 3D reconstruction showing the expression of CD31 and H2A.Z.1.
- (D) Sulfo-NHS-LC-biotin and CD31 staining of cortical sections from E15.5 *H2afz^{fl/fl}* and *H2afz^{cKO(Tek)}* mice.
- (E) Quantification of normalized intensity of sulfo-NHS-LC-biotin in CD31⁻ regions in (D).
- (F) Cortical sections from E15.5 *H2afz^{fl/fl}* and *H2afz^{cKO(Tek)}* mice were co-stained with MFSD2A and CD31 antibodies. Imapris 3D reconstruction showing the expression of MFSD2A co-localized with CD31.
- (G) Quantification of normalized intensity of MFSD2A in CD31⁺ cells in (F).
- (H) Cortical sections from E15.5 *H2afz^{fl/fl}* and *H2afz^{cKO(Tek)}* mice were co-stained with GLUT1 and CD31 antibodies. Imapris 3D reconstruction showing the expression of GLUT1 co-localized with CD31.
- (I) Quantification of normalized intensity of GLUT1 in CD31⁺ cells in (H).
- (J) E15.5 cerebrovascular ECs in *H2afz^{fl/fl}* and *H2afz^{cKO(Tek)}* mice were isolated via FACS and lysed for immunoblotting (IB) with the indicated antibodies.
- (K) Quantitation of the protein levels of MFSD2A, GLUT1, and CAV-1 in (J).
- (L) TEM images showing transcytotic vesicles in endothelium of E17.5 *H2afz^{fl/fl}* and *H2afz^{cKO(Tek)}* mice. Left: transcytotic vesicles are categorized into three types: luminal (arrows) or abluminal (arrowheads) membrane-connected and cytoplasmic vesicles (asterisks).
- (M) Quantification of transcytotic vesicular density in TEM images, normalized by EC area.
- (N) Glutamine (Gln)-Cy3 and VEGFR2 staining of cortical sections from P2 *H2afz^{fl/fl}* and *H2afz^{cKO(Tek)}* mice.
- (O) Quantification of normalized intensity of Gln-cy3 in CD31⁻ regions in (N).
- (P) Cortical sections from E15.5 *H2afz^{fl/fl}* and *H2afz^{cKO(Tek)}* mice were co-stained with β -catenin and CD31 antibodies.
- (Q) Quantification of ratio of nuclear- β -catenin⁺CD31⁺ cells in CD31⁺ cells.
- (R) E15.5 cerebrovascular ECs in *H2afz^{fl/fl}* and *H2afz^{cKO(Tek)}* mice were isolated via FACS and lysed for IB with the indicated antibodies.
- (S) Quantitation of the protein levels of TCF1 and LEF1 in (R).
- (T) bEnd.3 cells were infected with *FLAG-H2afz* and *HA-Ctnnb1* overexpression lentivirus for 3 days and harvested for anti-FLAG immunoprecipitation (IP) followed by IB with the indicated antibodies.
- (U) Quantitation of the protein levels of hemagglutinin (HA) and FLAG of IB group in (T).
- (V) bEnd.3 cells were infected with *HA-Ctnnb1* and *FLAG-H2afz* overexpression lentivirus for 3 days and harvested for anti-HA IP followed by IB with the indicated antibodies.
- (W) Quantitation of the protein levels of FLAG and HA of IB group in (V).

In (U) and (W), $n = 3$ independent repeated experiments. In (E), (G), (I), (K), (M), (O), (Q), and (S), $n = 6$ independent repeated experiments. Bars represent mean \pm SEM. Unpaired two-tailed *t* test: n.s., not significant, * $p < 0.05$, ** $p < 0.01$, *** $p < 0.001$. L, luminal; EC, endothelium; Ab, abluminal. See also Figures S9 and S10.

Materials availability

Reagents generated in this study are available, upon reasonable request, with a completed materials transfer agreement. All the reagents in this study are included in the [key resources table](#).

Data and code availability

- The raw sequence data generated in this study have been deposited in the Genome Sequence Archive Human⁷⁸ at the National Genomics Data Center (2020), Beijing Institute of Genomics (China National Center for Bioinformatics), Chinese Academy of Sciences, and the accession numbers are listed below. Human scRNA-seq data: HRA005468, HRA000714, HRA000715, HRA000718, and HRA000719; human scStereo-seq data⁹: HRA004776, HRA003401, HRA005014, HRA004685, HRA004686, HRA004968, HRA002261, HRA004969, and HRA004257. They are publicly accessible at <http://bigd.big.ac.cn/gsa-human>. Human MERFISH data reported in this paper have been deposited in the OMIX, China National Center for Bioinformatics/Beijing Institute of Genomics, Chinese Academy of Sciences (<https://ngdc.cncb.ac.cn/omix>; accession no. OMIX011810).
- This paper does not report original code.
- Any additional information required to reanalyze the data reported in this paper is available from the [lead contact](#) upon request.

ACKNOWLEDGMENTS

This work was supported by grants from the National Natural Science Foundation of China (32450088, 92368203, 92468302, 32230040, 32300671, 32300949, and 32222028), the National Key R&D Program of China (2024YFA1802600, 2024YFA1802202, 2023YFA1801500, 2024YFA1107500, and 2021YFA1101402), “Bingzhi” Postdoctoral Special Support Program (E251791131), Chinese Academy of Medical Sciences Innovation Fund for Medical Sciences (2024-I2M-3-025), Young Elite Scientist Sponsorship Program by China Association for Science and Technology (YESS20220104), and China Postdoctoral Science Foundation (2024T170917 and 2022T150645). We are grateful to Zhongshuang Lv and Xixia Li for helping with electron microscopy sample preparation and taking TEM images at the Center for Biological Imaging (CBI), Institute of Biophysics, Chinese Academy of Science. We thank the Chinese Brain Bank Center for providing the adult brain tissue.

AUTHOR CONTRIBUTIONS

Z.L., Y.L., J.D., and Jianwei Jiao designed the research; Z.L. and Y.L. performed RNA-seq; Z.H. was mainly responsible for data analysis, and C.W. provided some analysis assistance; Z.L. and Y.L. designed and performed experiments; Y.Z., R.L., L.J., Jin Jiao, and F.J. prepared the samples. For the MERFISH experiment, Z.L. and Y.L. performed frozen sectioning and mounting of samples, and B.Z. conducted the subsequent staining, imaging, and sequencing experiments; P.D. and J.Z. provided some guidance and help; Z.L., Y.L., Z.H., J.D., and Jianwei Jiao wrote the manuscript; Jianwei Jiao supervised the project and obtained funding support. All authors edited and proofread the manuscript.

DECLARATION OF INTERESTS

The authors declare no competing interests.

STAR★METHODS

Detailed methods are provided in the online version of this paper and include the following:

- [KEY RESOURCES TABLE](#)
- [EXPERIMENTAL MODEL AND STUDY PARTICIPANT DETAILS](#)
 - Human samples collection
 - Mice
 - Cell cultures
- [METHOD DETAILS](#)
 - Preparation of cell suspensions of tissue samples

- Fluorescence-activated cell sorting (FACS)
- scRNA-seq library preparation and sequencing
- MERFISH imaging experiment
- RNA amplification-based single molecule in situ hybridization (asm-FISH) assay
- Immunostaining
- Plasmid constructs
- Lentivirus packaging and infection
- Human ESCs differentiation to human NPCs and Neurons
- Co-culture of human ECs and human ESC-induced NPCs/ neurons
- In utero electroporation with PDGFD knockdown or overexpression and PDGFR inhibitor treatment
- Pericytes proliferation assay with human NPCs supernatant
- Pericytes proliferation assay with PDGFD and PDGFR inhibitor treatment
- Enzyme linked immunosorbent assay (ELISA)
- Transmission electron microscopy
- Embryonic BBB permeability assay
- Postnatal BBB permeability assay
- Glutamine metabolism and homeostasis assay
- Immunoprecipitation
- Western blotting
- Chromatin immunoprecipitation (ChIP)
- [QUANTIFICATION AND STATISTICAL ANALYSIS](#)
 - scRNA data processing
 - Spatial stereo-seq data pre-processing
 - Mapping cell types from scRNA-seq onto scStereo-seq
 - MERFISH data preprocessing and mapping cell types from scRNA-seq onto MERFISH
 - Correlation Analysis
 - Enrichment analysis
 - Gene expression pattern analysis
 - Gene expression quantification methods for scRNA-seq data
 - Cluster ratio analysis
 - Trajectory analysis
 - Analysis of public scRNA-seq datasets
 - Correlation Analysis
 - Cell-cell communication analysis
 - BBB scores
 - Cell-cell communication in spatial transcriptomics data
 - Cross-species analysis of endothelial cells
 - Comparison of pseudotime trajectories between human and mouse
 - Confocal imaging and statistical analysis

SUPPLEMENTAL INFORMATION

Supplemental information can be found online at <https://doi.org/10.1016/j.stem.2026.02.010>.

Received: July 11, 2025

Revised: January 15, 2026

Accepted: February 24, 2026

REFERENCES

1. Obermeier, B., Daneman, R., and Ransohoff, R.M. (2013). Development, maintenance and disruption of the blood-brain barrier. *Nat. Med.* *19*, 1584–1596. <https://doi.org/10.1038/nm.3407>.
2. Stenman, J.M., Rajagopal, J., Carroll, T.J., Ishibashi, M., McMahon, J., and McMahon, A.P. (2008). Canonical Wnt signaling regulates organ-specific assembly and differentiation of CNS vasculature. *Science* *322*, 1247–1250. <https://doi.org/10.1126/science.1164594>.
3. Daneman, R., Agalliu, D., Zhou, L., Kuhnert, F., Kuo, C.J., and Barres, B.A. (2009). Wnt/beta-catenin signaling is required for CNS, but not non-CNS, angiogenesis. *Proc. Natl. Acad. Sci. USA* *106*, 641–646. <https://doi.org/10.1073/pnas.0805165106>.

- Winkler, E.A., Kim, C.N., Ross, J.M., Garcia, J.H., Gil, E., Oh, I., Chen, L.Q., Wu, D., Catapano, J.S., Raygor, K., et al. (2022). A single-cell atlas of the normal and malformed human brain vasculature. *Science* 375, eabi7377. <https://doi.org/10.1126/science.abi7377>.
- Yang, A.C., Vest, R.T., Kern, F., Lee, D.P., Agam, M., Maat, C.A., Losada, P.M., Chen, M.B., Schaum, N., Khoury, N., et al. (2022). A human brain vascular atlas reveals diverse mediators of Alzheimer's risk. *Nature* 603, 885–892. <https://doi.org/10.1038/s41586-021-04369-3>.
- Garcia, F.J., Sun, N., Lee, H., Godlewski, B., Mathys, H., Galani, K., Zhou, B., Jiang, X., Ng, A.P., Mantero, J., et al. (2022). Single-cell dissection of the human brain vasculature. *Nature* 603, 893–899. <https://doi.org/10.1038/s41586-022-04521-7>.
- Wälchli, T., Ghobrial, M., Schwab, M., Takada, S., Zhong, H., Suntharalingham, S., Vetiska, S., Gonzalez, D.R., Wu, R., Rehrauer, H., et al. (2024). Single-cell atlas of the human brain vasculature across development, adulthood and disease. *Nature* 632, 603–613. <https://doi.org/10.1038/s41586-024-07493-y>.
- Chen, A., Liao, S., Cheng, M., Ma, K., Wu, L., Lai, Y., Qiu, X., Yang, J., Xu, J., Hao, S., et al. (2022). Spatiotemporal transcriptomic atlas of mouse organogenesis using DNA nanoball-patterned arrays. *Cell* 185, 1777–1792.e21. <https://doi.org/10.1016/j.cell.2022.04.003>.
- Li, Y., Li, Z., Wang, C., Yang, M., He, Z., Wang, F., Zhang, Y., Li, R., Gong, Y., Wang, B., et al. (2023). Spatiotemporal transcriptome atlas reveals the regional specification of the developing human brain. *Cell* 186, 5892–5909.e22. <https://doi.org/10.1016/j.cell.2023.11.016>.
- Sun, E.D., Zhou, O.Y., Hauptschein, M., Rappoport, N., Xu, L., Navarro Negredo, P., Liu, L., Rando, T.A., Zou, J., and Brunet, A. (2025). Spatial transcriptomic clocks reveal cell proximity effects in brain ageing. *Nature* 638, 160–171. <https://doi.org/10.1038/s41586-024-08334-8>.
- Choi, J., Li, J., Ferdous, S., Liang, Q.N., Moffitt, J.R., and Chen, R. (2023). Spatial organization of the mouse retina at single cell resolution by MERFISH. *Nat. Commun.* 14, 4929. <https://doi.org/10.1038/s41467-023-40674-3>.
- Korsunsky, I., Millard, N., Fan, J., Slowikowski, K., Zhang, F., Wei, K., Baglaenko, Y., Brenner, M., Loh, P.R., and Raychaudhuri, S. (2019). Fast, sensitive and accurate integration of single-cell data with Harmony. *Nat. Methods* 16, 1289–1296. <https://doi.org/10.1038/s41592-019-0619-0>.
- Di Bella, D.J., Habibi, E., Stickels, R.R., Scalia, G., Brown, J., Yadollahpour, P., Yang, S.M., Abbate, C., Biancalani, T., Macosko, E.Z., et al. (2021). Molecular logic of cellular diversification in the mouse cerebral cortex. *Nature* 595, 554–559. <https://doi.org/10.1038/s41586-021-03670-5>.
- Ben-Zvi, A., Lacoste, B., Kur, E., Andreone, B.J., Mayshar, Y., Yan, H., and Gu, C. (2014). Mfsd2a is critical for the formation and function of the blood-brain barrier. *Nature* 509, 507–511. <https://doi.org/10.1038/nature13324>.
- Sabbagh, M.F., Heng, J.S., Luo, C., Castanon, R.G., Nery, J.R., Rattner, A., Goff, L.A., Ecker, J.R., and Nathans, J. (2018). Transcriptional and epigenomic landscapes of CNS and non-CNS vascular endothelial cells. *eLife* 7, e36187. <https://doi.org/10.7554/eLife.36187>.
- Kalucka, J., de Rooij, L.P.M.H., Goveia, J., Rohlenova, K., Dumas, S.J., Meta, E., Conchinha, N.V., Taverna, F., Teuwen, L.A., Veys, K., et al. (2020). Single-Cell Transcriptome Atlas of Murine Endothelial Cells. *Cell* 180, 764–779.e20. <https://doi.org/10.1016/j.cell.2020.01.015>.
- Tata, M., and Ruhrberg, C. (2018). Cross-talk between blood vessels and neural progenitors in the developing brain. *Neuronal Signal.* 2, NS20170139. <https://doi.org/10.1042/ns20170139>.
- Peguera, B., Segarra, M., and Acker-Palmer, A. (2021). Neurovascular cross-talk coordinates the central nervous system development. *Curr. Opin. Neurobiol.* 69, 202–213. <https://doi.org/10.1016/j.conb.2021.04.005>.
- Tata, M., Ruhrberg, C., and Fantin, A. (2015). Vascularisation of the central nervous system. *Mech. Dev.* 138, 26–36. <https://doi.org/10.1016/j.mod.2015.07.001>.
- Puelles, L., Martínez-Marín, R., Melgarejo-Otalora, P., Ayad, A., Valavanis, A., and Ferran, J.L. (2019). Patterned Vascularization of Embryonic Mouse Forebrain, and Neuromeric Topology of Major Human Subarachnoidal Arterial Branches: A Prosomeric Mapping. *Front. Neuroanat.* 13, 59. <https://doi.org/10.3389/fnana.2019.00059>.
- Crouch, E.E., Bhaduri, A., Andrews, M.G., Cebrian-Silla, A., Diafos, L.N., Birrueta, J.O., Wedderburn-Pugh, K., Valenzuela, E.J., Bennett, N.K., Eze, U.C., et al. (2022). Ensembles of endothelial and mural cells promote angiogenesis in prenatal human brain. *Cell* 185, 3753–3769.e18. <https://doi.org/10.1016/j.cell.2022.09.004>.
- Strasser, G.A., Kaminker, J.S., and Tessier-Lavigne, M. (2010). Microarray analysis of retinal endothelial tip cells identifies CXCR4 as a mediator of tip cell morphology and branching. *Blood* 115, 5102–5110. <https://doi.org/10.1182/blood-2009-07-230284>.
- del Toro, R., Prahst, C., Mathivet, T., Siegfried, G., Kaminker, J.S., Larriève, B., Breant, C., Duarte, A., Takakura, N., Fukamizu, A., et al. (2010). Identification and functional analysis of endothelial tip cell-enriched genes. *Blood* 116, 4025–4033. <https://doi.org/10.1182/blood-2010-02-270819>.
- Zhao, Q., Eichten, A., Parveen, A., Adler, C., Huang, Y., Wang, W., Ding, Y., Adler, A., Nevins, T., Ni, M., et al. (2018). Single-Cell Transcriptome Analyses Reveal Endothelial Cell Heterogeneity in Tumors and Changes following Antiangiogenic Treatment. *Cancer Res.* 78, 2370–2382. <https://doi.org/10.1158/0008-5472.CAN-17-2728>.
- Goveia, J., Rohlenova, K., Taverna, F., Treps, L., Conradi, L.C., Pircher, A., Geldhof, V., de Rooij, L.P.M.H., Kalucka, J., Sokol, L., et al. (2020). An Integrated Gene Expression Landscape Profiling Approach to Identify Lung Tumor Endothelial Cell Heterogeneity and Angiogenic Candidates. *Cancer Cell* 37, 421. <https://doi.org/10.1016/j.ccell.2020.03.002>.
- Fleming, R.E., Crouch, E.C., Ruzicka, C.A., and Sly, W.S. (1993). Pulmonary carbonic anhydrase IV: developmental regulation and cell-specific expression in the capillary endothelium. *Am. J. Physiol.* 265, L627–L635. <https://doi.org/10.1152/ajplung.1993.265.6.L627>.
- Vanlandewijck, M., He, L., Mäe, M.A., Andrae, J., Ando, K., Del Gaudio, F., Nahar, K., Lebouvier, T., Laviña, B., Gouveia, L., et al. (2018). A molecular atlas of cell types and zonation in the brain vasculature. *Nature* 554, 475–480. <https://doi.org/10.1038/nature25739>.
- Zhao, Z., Nelson, A.R., Betsholtz, C., and Zlokovic, B.V. (2015). Establishment and Dysfunction of the Blood-Brain Barrier. *Cell* 163, 1064–1078. <https://doi.org/10.1016/j.cell.2015.10.067>.
- Miller, D.S. (2015). Regulation of ABC transporters blood-brain barrier: the good, the bad, and the ugly. *Adv. Cancer Res.* 125, 43–70. <https://doi.org/10.1016/bs.acr.2014.10.002>.
- Zeng, B., Liu, Z., Lu, Y., Zhong, S., Qin, S., Huang, L., Zeng, Y., Li, Z., Dong, H., Shi, Y., et al. (2023). The single-cell and spatial transcriptional landscape of human gastrulation and early brain development. *Cell Stem Cell* 30, 851–866.e7. <https://doi.org/10.1016/j.stem.2023.04.016>.
- Tuma, P.L., and Hubbard, A.L. (2003). Transcytosis: crossing cellular barriers. *Physiol. Rev.* 83, 871–932. <https://doi.org/10.1152/physrev.00001.2003>.
- Carmeliet, P., Ferreira, V., Breier, G., Pollefeyt, S., Kieckens, L., Gertsenstein, M., Fahrig, M., Vandenhoek, A., Harpal, K., Eberhardt, C., et al. (1996). Abnormal blood vessel development and lethality in embryos lacking a single VEGF allele. *Nature* 380, 435–439. <https://doi.org/10.1038/380435a0>.
- Stewart, P.A., and Wiley, M.J. (1981). Developing nervous tissue induces formation of blood-brain barrier characteristics in invading endothelial cells: a study using quail–chick transplantation chimeras. *Dev. Biol.* 84, 183–192. [https://doi.org/10.1016/0012-1606\(81\)90382-1](https://doi.org/10.1016/0012-1606(81)90382-1).
- Bystron, I., Blakemore, C., and Rakic, P. (2008). Development of the human cerebral cortex: Boulder Committee revisited. *Nat. Rev. Neurosci.* 9, 110–122. <https://doi.org/10.1038/nrn2252>.
- Cang, Z., Zhao, Y., Almet, A.A., Stabell, A., Ramos, R., Plikus, M.V., Atwood, S.X., and Nie, Q. (2023). Screening cell-cell communication in spatial transcriptomics via collective optimal transport. *Nat. Methods* 20, 218–228. <https://doi.org/10.1038/s41592-022-01728-4>.

36. Jin, S., Guerrero-Juarez, C.F., Zhang, L., Chang, I., Ramos, R., Kuan, C.H., Myung, P., Plikus, M.V., and Nie, Q. (2021). Inference and analysis of cell-cell communication using CellChat. *Nat. Commun.* *12*, 1088. <https://doi.org/10.1038/s41467-021-21246-9>.
37. Zhang, J., Woodhead, G.J., Swaminathan, S.K., Noles, S.R., McQuinn, E.R., Pisarek, A.J., Stocker, A.M., Mutch, C.A., Funatsu, N., and Chenn, A. (2010). Cortical neural precursors inhibit their own differentiation via N-cadherin maintenance of beta-catenin signaling. *Dev. Cell* *18*, 472–479. <https://doi.org/10.1016/j.devcel.2009.12.025>.
38. László, Z.I., and Lele, Z. (2022). Flying under the radar: CDH2 (N-cadherin), an important hub molecule in neurodevelopmental and neurodegenerative diseases. *Front. Neurosci.* *16*, 972059. <https://doi.org/10.3389/fnins.2022.972059>.
39. Daneman, R., Zhou, L., Kebede, A.A., and Barres, B.A. (2010). Pericytes are required for blood-brain barrier integrity during embryogenesis. *Nature* *468*, 562–566. <https://doi.org/10.1038/nature09513>.
40. LaRochelle, W.J., Jeffers, M., McDonald, W.F., Chillakuru, R.A., Giese, N.A., Lokker, N.A., Sullivan, C., Boldog, F.L., Yang, M., Vernet, C., et al. (2001). PDGF-D, a new protease-activated growth factor. *Nat. Cell Biol.* *3*, 517–521. <https://doi.org/10.1038/35074593>.
41. Li, L., Blumenthal, D.K., Terry, C.M., He, Y., Carlson, M.L., and Cheung, A.K. (2011). PDGF-induced proliferation in human arterial and venous smooth muscle cells: molecular basis for differential effects of PDGF isoforms. *J. Cell. Biochem.* *112*, 289–298. <https://doi.org/10.1002/jcb.22924>.
42. Armulik, A., Genové, G., Mäe, M., Nisancioglu, M.H., Wallgard, E., Niaudet, C., He, L., Norlin, J., Lindblom, P., Strittmatter, K., et al. (2010). Pericytes regulate the blood-brain barrier. *Nature* *468*, 557–561. <https://doi.org/10.1038/nature09522>.
43. Gerhardt, H., and Betsholtz, C. (2003). Endothelial-pericyte interactions in angiogenesis. *Cell Tissue Res.* *314*, 15–23. <https://doi.org/10.1007/s00441-003-0745-x>.
44. Hellström, M., Gerhardt, H., Kalén, M., Li, X., Eriksson, U., Wolburg, H., and Betsholtz, C. (2001). Lack of pericytes leads to endothelial hyperplasia and abnormal vascular morphogenesis. *J. Cell Biol.* *153*, 543–553. <https://doi.org/10.1083/jcb.153.3.543>.
45. Liu, H., Kennard, S., and Lilly, B. (2009). NOTCH3 expression is induced in mural cells through an autoregulatory loop that requires endothelial-expressed JAGGED1. *Circ. Res.* *104*, 466–475. <https://doi.org/10.1161/circresaha.108.184846>.
46. Wang, Y., Pan, L., Moens, C.B., and Appel, B. (2014). Notch3 establishes brain vascular integrity by regulating pericyte number. *Development* *141*, 307–317. <https://doi.org/10.1242/dev.096107>.
47. Doi, H., Iso, T., Sato, H., Yamazaki, M., Matsui, H., Tanaka, T., Manabe, I., Arai, M., Nagai, R., and Kurabayashi, M. (2006). Jagged1-selective notch signaling induces smooth muscle differentiation via a RBP-Jkappa-dependent pathway. *J. Biol. Chem.* *281*, 28555–28564. <https://doi.org/10.1074/jbc.M602749200>.
48. Penton, A.L., Leonard, L.D., and Spinner, N.B. (2012). Notch signaling in human development and disease. *Semin. Cell Dev. Biol.* *23*, 450–457. <https://doi.org/10.1016/j.semcdb.2012.01.010>.
49. Ladi, E., Nichols, J.T., Ge, W., Miyamoto, A., Yao, C., Yang, L.T., Boulter, J., Sun, Y.E., Kintner, C., and Weinmaster, G. (2005). The divergent DSL ligand Dll3 does not activate Notch signaling but cell autonomously attenuates signaling induced by other DSL ligands. *J. Cell Biol.* *170*, 983–992. <https://doi.org/10.1083/jcb.200503113>.
50. Matsuo, K., Taniguchi, K., Hamamoto, H., Ito, Y., Futaki, S., Inomata, Y., Shima, T., Asakuma, M., Lee, S.W., Tanaka, K., et al. (2019). Delta-like 3 localizes to neuroendocrine cells and plays a pivotal role in gastrointestinal neuroendocrine malignancy. *Cancer Sci.* *110*, 3122–3131. <https://doi.org/10.1111/cas.14157>.
51. Dohgu, S., Takata, F., Yamauchi, A., Nakagawa, S., Egawa, T., Naito, M., Tsuruo, T., Sawada, Y., Niwa, M., and Kataoka, Y. (2005). Brain pericytes contribute to the induction and up-regulation of blood-brain barrier functions through transforming growth factor-beta production. *Brain Res.* *1038*, 208–215. <https://doi.org/10.1016/j.brainres.2005.01.027>.
52. Van Hulle, C., Ince, S., Okonkwo, O.C., Bendlin, B.B., Johnson, S.C., Carlsson, C.M., Asthana, S., Love, S., Blennow, K., Zetterberg, H., et al. (2024). Elevated CSF angiopoietin-2 correlates with blood-brain barrier leakiness and markers of neuronal injury in early Alzheimer’s disease. *Transl. Psychiatry* *14*, 3. <https://doi.org/10.1038/s41398-023-02706-w>.
53. Maisonpierre, P.C., Suri, C., Jones, P.F., Bartunkova, S., Wiegand, S.J., Radziejewski, C., Compton, D., McClain, J., Aldrich, T.H., Papadopoulos, N., et al. (1997). Angiopoietin-2, a natural antagonist for Tie2 that disrupts in vivo angiogenesis. *Science* *277*, 55–60. <https://doi.org/10.1126/science.277.5322.55>.
54. Zobel, K., Hansen, U., and Galla, H.J. (2016). Blood-brain barrier properties in vitro depend on composition and assembly of endogenous extracellular matrices. *Cell Tissue Res.* *365*, 233–245. <https://doi.org/10.1007/s00441-016-2397-7>.
55. Otis, E.M., and Brent, R. (1954). Equivalent ages in mouse and human embryos. *Anat. Rec.* *120*, 33–63. <https://doi.org/10.1002/ar.1091200104>.
56. Sugihara, R., Kato, Y., Mori, T., and Kawahara, Y. (2022). Alignment of single-cell trajectory trees with CAPITAL. *Nat. Commun.* *13*, 5972. <https://doi.org/10.1038/s41467-022-33681-3>.
57. Nagano, H., Ito, S., Masuda, T., and Ohtsuki, S. (2022). Effect of Insulin Receptor-Knockdown on the Expression Levels of Blood-Brain Barrier Functional Proteins in Human Brain Microvascular Endothelial Cells. *Pharm. Res.* *39*, 1561–1574. <https://doi.org/10.1007/s11095-021-03131-8>.
58. Rispal, J., Baron, L., Beaulieu, J.F., Chevillard-Briet, M., Trouche, D., and Escaffit, F. (2019). The H2A.Z histone variant integrates Wnt signaling in intestinal epithelial homeostasis. *Nat. Commun.* *10*, 1827. <https://doi.org/10.1038/s41467-019-09899-z>.
59. Hu, G., Cui, K., Northrup, D., Liu, C., Wang, C., Tang, Q., Ge, K., Levens, D., Crane-Robinson, C., and Zhao, K. (2013). H2A.Z facilitates access of active and repressive complexes to chromatin in embryonic stem cell self-renewal and differentiation. *Cell Stem Cell* *12*, 180–192. <https://doi.org/10.1016/j.stem.2012.11.003>.
60. Nekrasov, M., Amrichova, J., Parker, B.J., Soboleva, T.A., Jack, C., Williams, R., Huttley, G.A., and Tremethick, D.J. (2012). Histone H2A.Z inheritance during the cell cycle and its impact on promoter organization and dynamics. *Nat. Struct. Mol. Biol.* *19*, 1076–1083. <https://doi.org/10.1038/nsmb.2424>.
61. Zhang, D., Hua, Z., and Li, Z. (2024). The role of glutamate and glutamine metabolism and related transporters in nerve cells. *CNS Neurosci. Ther.* *30*, e14617. <https://doi.org/10.1111/cns.14617>.
62. Xiang, J., Ennis, S.R., Abdelkarim, G.E., Fujisawa, M., Kawai, N., and Keep, R.F. (2003). Glutamine transport at the blood-brain and blood-cerebrospinal fluid barriers. *Neurochem. Int.* *43*, 279–288. [https://doi.org/10.1016/s0197-0186\(03\)00013-5](https://doi.org/10.1016/s0197-0186(03)00013-5).
63. Andersen, J.V. (2025). The Glutamate/GABA-Glutamine Cycle: Insights, Updates, and Advances. *J. Neurochem.* *169*, e70029. <https://doi.org/10.1111/jnc.70029>.
64. Hussain, B., Fang, C., Huang, X., Feng, Z., Yao, Y., Wang, Y., and Chang, J. (2022). Endothelial β -Catenin Deficiency Causes Blood-Brain Barrier Breakdown via Enhancing the Paracellular and Transcellular Permeability. *Front. Mol. Neurosci.* *15*, 895429. <https://doi.org/10.3389/fnmol.2022.895429>.
65. Shen, T., Ji, F., Wang, Y., Lei, X., Zhang, D., and Jiao, J. (2018). Brain-specific deletion of histone variant H2A.z results in cortical neurogenesis defects and neurodevelopmental disorder. *Nucleic Acids Res.* *46*, 2290–2307. <https://doi.org/10.1093/nar/gkx1295>.
66. Alahmari, A. (2021). Blood-Brain Barrier Overview: Structural and Functional Correlation. *Neural Plast.* *2021*, 6564585. <https://doi.org/10.1155/2021/6564585>.
67. Goasdoué, K., Miller, S.M., Colditz, P.B., and Björkman, S.T. (2017). Review: The blood-brain barrier; protecting the developing fetal brain. *Placenta* *54*, 111–116. <https://doi.org/10.1016/j.placenta.2016.12.005>.
68. Chen, J., Luo, Y., Hui, H., Cai, T., Huang, H., Yang, F., Feng, J., Zhang, J., and Yan, X. (2017). CD146 coordinates brain endothelial cell-pericyte

- communication for blood-brain barrier development. *Proc. Natl. Acad. Sci. USA* *114*, E7622–E7631. <https://doi.org/10.1073/pnas.1710848114>.
69. Wang, Y., Rattner, A., Zhou, Y., Williams, J., Smallwood, P.M., and Nathans, J. (2012). *Norrin/Frizzled4* signaling in retinal vascular development and blood brain barrier plasticity. *Cell* *151*, 1332–1344. <https://doi.org/10.1016/j.cell.2012.10.042>.
70. Dave, J.M., Mirabella, T., Weatherbee, S.D., and Greif, D.M. (2018). Pericyte ALK5/TIMP3 Axis Contributes to Endothelial Morphogenesis in the Developing Brain. *Dev. Cell* *47*, 388–389. <https://doi.org/10.1016/j.devcel.2018.10.019>.
71. Schumacher, U., and Mollgård, K. (1997). The multidrug-resistance P-glycoprotein (Pgp, MDR1) is an early marker of blood-brain barrier development in the microvessels of the developing human brain. *Histochem. Cell Biol.* *108*, 179–182. <https://doi.org/10.1007/s004180050159>.
72. Virgintino, D., Robertson, D., Benagiano, V., Errede, M., Bertossi, M., Ambrosi, G., and Roncali, L. (2000). Immunogold cytochemistry of the blood-brain barrier glucose transporter GLUT1 and endogenous albumin in the developing human brain. *Brain Res., Dev. Brain Res.* *123*, 95–101. [https://doi.org/10.1016/s0165-3806\(00\)00086-9](https://doi.org/10.1016/s0165-3806(00)00086-9).
73. Hogan, K.A., Ambler, C.A., Chapman, D.L., and Bautch, V.L. (2004). The neural tube patterns vessels developmentally using the VEGF signaling pathway. *Development* *131*, 1503–1513. <https://doi.org/10.1242/dev.01039>.
74. Kim, H.J., Cheng, P., Trivisano, S., Weldy, C., Monteiro, J.P., Kundu, R., Nguyen, T., Sharma, D., Shi, H., Lin, Y., et al. (2023). Molecular mechanisms of coronary artery disease risk at the PDGFD locus. *Nat. Commun.* *14*, 847. <https://doi.org/10.1038/s41467-023-36518-9>.
75. Dadone-Montaudié, B., Alberti, L., Duc, A., Delespaul, L., Lesluyes, T., Pérot, G., Lançon, A., Paindavoine, S., Di Mauro, I., Blay, J.Y., et al. (2018). Alternative PDGFD rearrangements in dermatofibrosarcomas protuberans without PDGFB fusions. *Mod. Pathol.* *31*, 1683–1693. <https://doi.org/10.1038/s41379-018-0089-4>.
76. Lindahl, P., Johansson, B.R., Levéen, P., and Betsholtz, C. (1997). Pericyte loss and microaneurysm formation in PDGF-B-deficient mice. *Science* *277*, 242–245. <https://doi.org/10.1126/science.277.5323.242>.
77. Tallquist, M.D., French, W.J., and Soriano, P. (2003). Additive effects of PDGF receptor beta signaling pathways in vascular smooth muscle cell development. *PLoS Biol.* *1*, E52. <https://doi.org/10.1371/journal.pbio.0000052>.
78. Wang, Y., Song, F., Zhu, J., Zhang, S., Yang, Y., Chen, T., Tang, B., Dong, L., Ding, N., Zhang, Q., et al. (2017). GSA: Genome Sequence Archive. *Genomics Proteomics Bioinformatics* *15*, 14–18. <https://doi.org/10.1016/j.gpb.2017.01.001>.
79. Hao, Y., Hao, S., Andersen-Nissen, E., Mauck, W.M., 3rd, Zheng, S., Butler, A., Lee, M.J., Wilk, A.J., Darby, C., Zager, M., et al. (2021). Integrated analysis of multimodal single-cell data. *Cell* *184*, 3573–3587.e29. <https://doi.org/10.1016/j.cell.2021.04.048>.
80. McGinnis, C.S., Murrow, L.M., and Gartner, Z.J. (2019). DoubletFinder: Doublet Detection in Single-Cell RNA Sequencing Data Using Artificial Nearest Neighbors. *Cell Syst.* *8*, 329–337.e4. <https://doi.org/10.1016/j.cels.2019.03.003>.
81. Zhou, Y., Zhou, B., Pache, L., Chang, M., Khodabakhshi, A.H., Tanaseichuk, O., Benner, C., and Chanda, S.K. (2019). Metascape provides a biologist-oriented resource for the analysis of systems-level datasets. *Nat. Commun.* *10*, 1523. <https://doi.org/10.1038/s41467-019-09234-6>.
82. Bunis, D.G., Andrews, J., Fragiadakis, G.K., Burt, T.D., and Sirota, M. (2021). dittoSeq: universal user-friendly single-cell and bulk RNA sequencing visualization toolkit. *Bioinformatics* *36*, 5535–5536. <https://doi.org/10.1093/bioinformatics/btaa1011>.
83. Wickham, H. (2009). *Ggplot2: Elegant Graphics for Data Analysis* (Springer). <https://doi.org/10.1007/978-0-387-98141-3>.
84. Qiu, X., Hill, A., Packer, J., Lin, D., Ma, Y.A., and Trapnell, C. (2017). Single-cell mRNA quantification and differential analysis with Censur. *Nat. Methods* *14*, 309–315. <https://doi.org/10.1038/nmeth.4150>.
85. Gong, C., Li, S., Wang, L., Zhao, F., Fang, S., Yuan, D., Zhao, Z., He, Q., Li, M., Liu, W., et al. (2024). SAW: an efficient and accurate data analysis workflow for Stereo-seq spatial transcriptomics. *GigaByte* *2024*, gigabyte111. <https://doi.org/10.46471/gigabyte.111>.
86. Biancalani, T., Scalia, G., Buffoni, L., Avasthi, R., Lu, Z., Sanger, A., Tokcan, N., Vanderburg, C.R., Segerstolpe, Å., Zhang, M., et al. (2021). Deep learning and alignment of spatially resolved single-cell transcriptomes with Tangram. *Nat. Methods* *18*, 1352–1362. <https://doi.org/10.1038/s41592-021-01264-7>.
87. Pachitariu, M., and Stringer, C. (2022). Cellpose 2.0: how to train your own model. *Nat. Methods* *19*, 1634–1641. <https://doi.org/10.1038/s41592-022-01663-4>.
88. Moses, L., Einarsson, P.H., Jackson, K., Luebbert, L., Boeshaghi, A.S., Antonsson, S., Bray, N., Melsted, P., and Pachter, L. (2023). Voyager: exploratory single-cell genomics data analysis with geospatial statistics. Preprint at bioRxiv. <https://doi.org/10.1101/2023.07.20.549945>.
89. Li, Y., Li, Z., Yang, M., Wang, F., Zhang, Y., Li, R., Li, Q., Gong, Y., Wang, B., Fan, B., et al. (2022). Decoding the temporal and regional specification of microglia in the developing human brain. *Cell Stem Cell* *29*, 620–634.e6. <https://doi.org/10.1016/j.stem.2022.02.004>.
90. Lin, C., Jiang, M., Liu, L., Chen, X., Zhao, Y., Chen, L., Hong, Y., Wang, X., Hong, C., Yao, X., et al. (2021). Imaging of individual transcripts by amplification-based single-molecule fluorescence in situ hybridization. *N. Biotechnol.* *67*, 116–123. <https://doi.org/10.1016/j.nbt.2020.12.001>.
91. Li, Y., and Jiao, J. (2017). Histone chaperone HIRA regulates neural progenitor cell proliferation and neurogenesis via β -catenin. *J. Cell Biol.* *216*, 1975–1992. <https://doi.org/10.1083/jcb.201610014>.
92. Li, Y., and Jiao, J. (2020). Deficiency of TRPM2 leads to embryonic neurogenesis defects in hyperthermia. *Sci. Adv.* *6*, eaay6350. <https://doi.org/10.1126/sciadv.aay6350>.
93. Huang, F., Wang, M., Yang, T., Cai, J., Zhang, Q., Sun, Z., Wu, X., Zhang, X., Zhu, W., Qian, H., et al. (2014). Gastric cancer-derived MSC-secreted PDGF-DD promotes gastric cancer progression. *J. Cancer Res. Clin. Oncol.* *140*, 1835–1848. <https://doi.org/10.1007/s00432-014-1723-2>.
94. Zhang, J., Zhang, H., Chen, Y., Fu, J., Lei, Y., Sun, J., and Tang, B. (2019). Platelet-derived growth factor D promotes the angiogenic capacity of endothelial progenitor cells. *Mol. Med. Rep.* *19*, 125–132. <https://doi.org/10.3892/mmr.2018.9692>.
95. Bi, Q., Wang, C., Cheng, G., Chen, N., Wei, B., Liu, X., Li, L., Lu, C., He, J., Weng, Y., et al. (2022). Microglia-derived PDGFB promotes neuronal potassium currents to suppress basal sympathetic tonicity and limit hypertension. *Immunity* *55*, 1466–1482.e9. <https://doi.org/10.1016/j.immuni.2022.06.018>.
96. Wang, Z., Liu, C.H., Huang, S., Fu, Z., Tomita, Y., Britton, W.R., Cho, S.S., Chen, C.T., Sun, Y., Ma, J.X., et al. (2020). Wnt signaling activates MFSD2A to suppress vascular endothelial transcytosis and maintain blood-retinal barrier. *Sci. Adv.* *6*, eaba7457. <https://doi.org/10.1126/sciadv.aba7457>.
97. Segarra, M., Aburto, M.R., Cop, F., Llaó-Cid, C., Härtl, R., Damm, M., Bethani, I., Parrilla, M., Husainie, D., Schänzer, A., et al. (2018). Endothelial Dab1 signaling orchestrates neuro-glia-vessel communication in the central nervous system. *Science* *361*, eaao2861. <https://doi.org/10.1126/science.aao2861>.
98. Li, Z., Li, Y., and Jiao, J. (2019). Neural progenitor cells mediated by H2A.Z.2 regulate microglial development via Cxcl14 in the embryonic brain. *Proc. Natl. Acad. Sci. USA* *116*, 24122–24132. <https://doi.org/10.1073/pnas.1913978116>.
99. Leek, J.T., Johnson, W.E., Parker, H.S., Jaffe, A.E., and Storey, J.D. (2012). The sva package for removing batch effects and other unwanted variation in high-throughput experiments. *Bioinformatics* *28*, 882–883. <https://doi.org/10.1093/bioinformatics/bts034>.

STAR★METHODS

KEY RESOURCES TABLE

REAGENT or RESOURCE	SOURCE	IDENTIFIER
Antibodies		
mouse anti-CD31	Abcam	Cat #: ab9498; RRID: AB_307284
guinea pig anti-CD31	Synaptic Systems	Cat #: HS-351004
rat anti-CD31	BD Biosciences	Cat #: 553370; RRID: AB_394816
rabbit anti-MFSD2A	Cell Signaling Technology	Cat #: 80302S
rabbit anti-SLC1A4	Novus	Cat #: NBP2-38226; RRID: AB_3297688
rabbit anti-ABCG2	Abcam	Cat #: ab207732
mouse anti-CLAUDIN5	Invitrogen	Cat #: 35-2500; RRID: AB_87321
rabbit anti-CADHERIN-2	Cell Signaling Technology	Cat #: 13116T
goat anti-SOX2	R&D Systems	Cat #: AF2018; RRID: AB_355110
mouse anti-TUJ1	Millipore	Cat #: MAB1637; RRID: AB_2210524
rabbit anti-c-JUN	Cell Signaling Technology	Cat # 9165; RRID: AB_2130165
mouse anti-Human NESTIN	R&D Systems	Cat #: MAB1259; RRID: AB_2251304
rabbit anti-GLUT-1	Millipore	Cat #: 07-1401; RRID: AB_1587074
goat anti-PDGFRB	R&D Systems	Cat #: AF385; RRID: AB_355339
rabbit anti-KI67	Abcam	Cat #: ab15580; RRID: AB_443209
rabbit anti-PDGFD	Abcam	Cat #: ab181845
goat anti-SOX2	R&D Systems	Cat #: AF2018; RRID: AB_355110
rabbit anti-TGFB1	Abcam	Cat #: ab215715; RRID: AB_2893156
mouse anti-TGFBR2	Proteintech	Cat #: 66636-1-Ig; RRID: AB_2881995
rabbit anti-ANGPT2	Abcam	Cat #: ab276042
rabbit anti-TIE2	Abcam	Cat #: ab24859; RRID: AB_2255983
mouse anti-COL1A1	Proteintech	Cat #: 66761-1-Ig; RRID: AB_2882107
rabbit anti-ITGB1	Atlas Antibodies	Cat #: HPA059297; RRID: AB_2732634
rat anti-PDGFB	Abcam	Cat #: ab107101
mouse anti-INSR	Invitrogen	Cat #: MA5-13783; RRID: AB_10985120
rabbit anti-H2A.Z.1	Active Motif	Cat #: 39943; RRID: AB_2793401
Isolectin B4	Fisher scientific	Cat #: NC9918852
rabbit anti-VEGFR2	Cell Signaling Technology	Cat # 2279; RRID: AB_2212507
mouse anti-Flag	Sigma-Aldrich	Cat #: F1804; RRID: AB_262044
rabbit anti-HA	Cell Signaling Technology	Cat #: 3724; RRID: AB_1549585
rabbit anti- β -catenin	Cell Signaling Technology	Cat #:8480; RRID: AB_11127855
rabbit anti-LEF1	Cell Signaling Technology	Cat #: 2230; RRID: AB_823558
rabbit anti-TCF1	Cell Signaling Technology	Cat #: 2203; RRID: AB_2199302
rabbit anti-CAV-1	Cell Signaling Technology	Cat #: 3267; RRID: AB_2275453
rabbit anti- β -actin	Proteintech	Cat #: 20536-1-AP; RRID: AB_10700003
PE rat anti-mouse-CD31	Biolegend	Cat #: 102408; RRID: AB_312903
PE mouse anti-human-CD31	Biolegend	Cat #: 303106; RRID: AB_314331
Biological samples		
See Table S1	this paper	N/A
Chemicals, peptides, and recombinant proteins		
Alexa Fluor™ 555 Cadaverine	Invitrogen	Cat #: A30677
EZ-link Sulfo-NHS-LC-Biotin	Thermo Fisher Scientific	Cat #: A39257
Glutamine-Cy3	RuixiBio	Cat #: R-R-0213
PDGFD ELISA Kit	Abebio	Cat #: AE28224HU

(Continued on next page)

Continued

REAGENT or RESOURCE	SOURCE	IDENTIFIER
PDGF-DD Protein	MCE	Cat #: HY-P7280
PDGFR inhibitor	Selleck	Cat #: S1536
Horseradish peroxidase (HRP)	Sigma-Aldrich	Cat #: P8250-5KU
3,3'-diaminobenzidine (DAB)	Sigma-Aldrich	Cat #: D8001
SlowFade Gold Antifade Mountant	Thermo Fisher Scientific	Cat #: S36940
Anti-HA-Magnetic Beads	MBL	Cat #: M132-11
Anti-DDDDKmAb-Magnetic Beads	MBL	Cat #: M185-11
Endothelial Cell Medium	ScienCell	Cat #: 1001
Matrigel Matrix	Corning	Cat #: 354277
Essential 8™ Flex medium	GIBCO	Cat #: A1517001
DMEM/F12 medium	Invitrogen	Cat #: 11330-032
Neurobasal medium	Invitrogen	Cat #: 21103-049
N-2 supplement	GIBCO	Cat #: 17502-048
B27 supplement without vitamin A	GIBCO	Cat #: 12587010
Gluta MAX	GIBCO	Cat #: 35050061
Leukemia Inhibitory Factor human	Millipore	Cat #: LIF1010
Dorsomorphin	Sigma-Aldrich	Cat #: P5499
SB431542	Tocris Bioscience	Cat #: 1614
CHIR99021	Stemgent	Cat #: 04-0004-10
Compound E	R&D Systems	Cat #: 6476
Accutase	Thermo Fisher Scientific	Cat #: A1110501
dbcAMP	Selleck	Cat #: S7858
ascorbic acid	Sigma-Aldrich	Cat #: A8960
BDNF	PeprTech	Cat #: 450-02
GDNF	PeprTech	Cat #: 450-10
DMEM, high glucose	GIBCO	Cat #: 11995-065
Fetal Bovine Serum (FBS)	GIBCO	Cat #: 10099-141C
Penicillin/Streptomycin	Invitrogen, 15070063	Cat #: 15070063
Pericyte Medium	ScienCell	Cat #: 1201
Collagenase II	Sigma-Aldrich	Cat #: C6885-1G
DNase I	Roche	Cat #: 11284932001
Dispase II	Roche	Cat #: 04942078001
Red Blood Cell Lysis Buffer	Invitrogen	Cat #: 00-4333-57
Collagen, Type I solution from rat tail	Sigma-Aldrich	Cat #: C3867-1VL
Quick antigen repair solution for frozen sections	Beyotime	Cat #: P0090

Deposited data

Human scRNA-seq data	this paper	GSA-human: HRA005468, HRA000714, HRA000715, HRA000718, HRA000719
MERFISH data	this paper	OMIX-human: OMIX011810
Human scStereo-seq data	our published paper ⁹	GSA-human: HRA004776, HRA003401, HRA005014, HRA004685, HRA004686, HRA004968, HRA002261, HRA004969, HRA004257

Experimental models: Cell lines

H9	WiCell Research Institute	WA09
hCMEC/D3	Millipore	Cat #: SCC066
human brain vascular pericyte	ScienCell	Cat #: 1200
bEnd.3	ATCC	Cat #: CRL-2299

(Continued on next page)

Continued

REAGENT or RESOURCE	SOURCE	IDENTIFIER
Experimental models: Organisms/strains		
<i>H2afz/H2afv</i> floxed mice (B6.Cg- <i>H2az1^{tm1.1Hko} H2az2^{tm1.1Hko}</i>)	RIKEN BioResource Research Center	Stock No: RBRC05765
<i>Tek-Cre</i> mice	Jackson Laboratory	Stock No: 008863
Oligonucleotides		
See Table S7	this paper	N/A
Recombinant DNA		
<i>Flag-Control</i>	this paper	N/A
<i>Flag-Pdgfd</i>	this paper	N/A
<i>Flag-H2afz</i>	this paper	N/A
<i>HA-Ctnnb1</i>	this paper	N/A
Software and algorithms		
ZEN	Zeiss	https://www.zeiss.com/microscopy/en/products/software/zeiss-zen.html
GraphPad Prism	GraphPad	https://www.graphpad.com
Photoshop CC	Adobe	https://www.adobe.com/products/photoshop.html
Cell Ranger (v5.0.1)	10x Genomics	https://www.10xgenomics.com
Seurat (v4.3.0)	Hao et al. ⁷⁹	https://satijalab.org/seurat/
DoubletFinder (v2.0.3)	McGinnis et al. ⁸⁰	https://github.com/chris-mcginnis-ucsf/DoubletFinder
Harmony (v0.1.0)	Korsunsky et al. ¹²	https://github.com/immunogenomics/harmony
Webserver	Zhou et al. ⁸¹	https://metascape.org/gp/index.html#/main/step1
dittoSeq (v1.6.0)	Bunis et al. ⁸²	https://github.com/dtm2451/dittoSeq
ggplot2 (v3.4.4)	Wickham ⁸³	https://ggplot2.tidyverse.org/
Monocle2 (v2.14.0)	Qiu et al. ⁸⁴	https://cole-trapnell-lab.github.io/monocle-release/docs/
CellChat (v1.1.3)	Jin et al. ³⁶	https://github.com/sqjin/CellChat
Pheatmap_1.0.12	N/A	https://rdr.io/cran/pheatmap/
R	Gong et al. ⁸⁵	https://www.r-project.org/
StereoMap (v2.1.0)	N/A	https://www.stomics.tech/products/BioinfoTools/OfflineSoftware/list.html
SAW (v6.1)	Gong et al. ⁸⁵	https://github.com/STOMics/SAW
Tangram (v1.0.4)	Biancalani et al. ⁸⁶	https://github.com/broadinstitute/Tangram
CAPITAL (v1.1.2)	Sugihara et al. ⁸⁶	https://github.com/ykat0/capital
mousipy (v0.1.5)	Stefan Peidli	https://github.com/stefanpeidli/mousipy
Cellpose (v2.2.3)	Pachitariu and Stringer ⁸⁷	https://github.com/MouseLand/cellpose
Voyager (v1.8.1)	Moses et al. ⁸⁸	https://github.com/pachterlab/voyager
COMMOT (v 0.0.3)	Cang et al. ⁸⁵	https://github.com/zcang/COMMOT

EXPERIMENTAL MODEL AND STUDY PARTICIPANT DETAILS

Human samples collection

The normally developing human fetuses were obtained at Peking University Third Hospital and Tongzhou Maternal and Child Health Hospital of Beijing. The collection and utilization of human fetal materials strictly comply with laws and ethical regulations, and are approved by the Reproductive Study Ethics Committee of Peking University Third Hospital and the institutional review board (ethics committee) of the Institute of Zoology. The informed consent was signed with the donors before the collection of tissue from human fetuses. The donor signs an informed consent form before collecting human fetal tissue. All plans comply with the Interim Measures for the Administration of Human Genetic Resources, administered by the Ministry of Science and Technology of China. The detailed information of human samples, such as developmental stage, gender, and replication, is shown in [Table S1](#). The adult cerebral cortex tissues of human were provided by the Chinese Brain Bank Center.

Mice

H2afz/H2afv floxed mice (B6.Cg-*H2az1^{tm1.1Hko}* *H2az2^{tm1.1Hko}*) were purchased from RIKEN BioResource Research Center through the National Bio-Resource Project of the Ministry of Education, Culture, Sports, Science and Technology. To generate *H2afz* floxed mice (*H2afz^{fl/fl}*), C57BL/6J mice (purchased from Vital River) were crossed with *H2afz/H2afv* floxed mice, and then the F1 generations were mated to each other to obtain *H2afz^{fl/fl}* mice. *H2afz^{CKO(Tek)}* (conditional deletion) mice were generated by crossing *H2afz^{fl/fl}* mice with *Tek-Cre* mice (obtained from The Jackson Laboratory). All experimental procedures followed by the Animal Committee of the Institute of Zoology, Chinese Academy of Sciences, China.

Cell cultures

H9 human ESCs were cultured in Matrigel Matrix (Corning, #: 354277)-coated 6-well plates (Corning) in Essential 8™ Flex medium (GIBCO, #: A1517001). The human brain microvascular endothelial cell line hCMEC/D3 cells were maintained in Endothelial Cell Medium (ScienCell, #: 1001). The human brain vascular pericytes were cultured in Collagen, Type I solution from rat tail (Sigma-Aldrich, #: C3867-1VL)-coated 10cm dish (Corning) in Pericyte Medium (ScienCell, #: 1201). The mouse brain endothelial cell line bEnd.3 cells were cultured in DMEM (GIBCO, #: 11995-065) containing 10% FBS (GIBCO, #: 10099-141C) and 1% Penicillin/Streptomycin (Invitrogen, 15070063). The medium was changed every two days and all cells were cultured in 5% CO₂ under 37 °C.

METHOD DETAILS

Preparation of cell suspensions of tissue samples

For human, the embryonic heads and the cerebral cortex of the brain were separated by stereomicroscope with dissecting forceps in cold artificial cerebrospinal fluid. The tissues were cut into pieces and digested in DMEM (high glucose) (GIBCO, #: 11995-065) containing 5 mg/ml collagenase II (Sigma-Aldrich, #: C6885-1G) and 30 U/ml DNase I (Roche, #: 11284932001) for 15 min in 37 °C incubator with shaking table. Then 2 U/ml Dispase II (Roche, #: 04942078001) was added at 37 °C for 15 min. The cell suspension was pipetted into single cells. After 300 g centrifugation, the erythrocytes were removed using lysis buffer (Invitrogen, #: 00-4333-57), the cell suspension was next passed through a 40 μm cell filter for subsequent experiments.

For the digestion of head and cerebral cortex of mouse, we adapted previous study.⁶⁸ Specifically, the tissues were cut into small pieces using disinfected blades and were digested in DMEM (high glucose) with 5 mg/ml collagenase II and 30 U/ml DNase I for 30-60 min at 37 °C. The mixture was centrifuged at 300 g for 5 min and washed with DMEM (high glucose). Next, 25% BSA was added and centrifuged at 1,360 g for 10 min. The myelin on the top was carefully removed, and the cells were washed with DMEM and centrifuged at 300 g for 5 min. The cells then were digested with 2 U/ml Dispase II and 5 mg/ml collagenase II for 30 min at 37 °C. After spinning for 5 min at 300 g to remove the enzymes, cell suspension was passed through a 40 μm cell filter for subsequent experiments.

Fluorescence-activated cell sorting (FACS)

In order to enrich endothelial cells and other vascular related cells, we referred to our previously published protocol.⁸⁹ Briefly, the cell suspension was washed three times with DPBS (Gibco, #: C14190500CP) and centrifuged at 300 g for 5 minutes each time. The cells were incubated on ice for 30 min with PE-conjugated anti-human CD31 (BioLegend, #: 303106) or PE-conjugated anti-mouse CD31 (BioLegend, #: 102408) to label endothelial cells (1:100) in FACS buffer (2% FBS in DPBS). Cells were washed two times with FACS buffer and 7-AAD (BioLegend, #: 420403) was added to exclude dead cells before subjected to FACS. Cells were sorted with a Beckman Coulter MoFlo XDP and the data were analyzed with the FlowJo software (Version: 10.4).

scRNA-seq library preparation and sequencing

scRNA-seq library preparation and sequencing referred to the previous protocol.⁹ In brief, the cells obtained from directly digested cells or FACS sorted cells were loaded on Chromium Single cell Controller (10x Genomics) with the Chromium Single cell 3'kit V3 to acquire about 8000 cells each sample. Then, the libraries were constructed and sequenced on an Illumina NovaSeq 6000 platform (Illumina, San Diego) with a read length of 26bp for read 1 (cell barcode and UMI), 8 bp i7 index read (sample barcode), and 98 bp for read 2 (actual RNA read) by Annoroad Gene Technology Co., Ltd (Beijing, China) and CapitalBio Technology Co., Ltd (Beijing, China). Firstly, the reads were sequenced in fast run mode, which allowed for fine-tuning sample ratios in the following high-output runs. Combining data from both flow cells, each cell generated approximately > 40000 reads.

MERFISH imaging experiment

The MERFISH experiment was conducted through the Vizgen MERSCOPE technology laboratory service. Compared with other spatially resolved single-cell transcriptomics, Vizgen MERSCOPE technology has been shown to provide high specificity and sensitivity even with larger gene panel sizes (1000 genes). Fresh frozen human embryonic/fetal samples of head were cut into 10 μm-thick sections on a cryostat at -20 °C and placed onto a MERSCOPE slide (Vizgen 20400001). The tissue sections were fixed with 4% PFA in 1× PBS for 30 minutes, washed 3 times with 5 ml 1× PBS and incubated with 70% ethanol at 4 °C overnight for tissue permeabilization. Samples were then hybridized with a custom designed MERSCOPE Gene Panel Mix consisting of 1000 genes (Vizgen 20300141) in a 37 °C incubator for 36 hours. Following incubation, the tissues were washed with 5 ml formamide wash buffer at 47 °C for 30 minutes, twice and embedded into a hydrogel using the Gel Embedding Premix (Vizgen 20300004), ammonium

persulfate (Sigma-Aldrich, 09913-100 G) and TEMED (N,N,N', N'-tetramethylethylenediamine) (Sigma, T7024-25ML) from the MERSCOPE Sample Prep Kit (10400012). After the gel mix solution solidified, the samples were cleared with clearing solution consisting of 50 μ l Proteinase K (NEB, P8107S) and 5 ml of Clearing Premix (Vizgen 20300003) at 37 °C overnight. After removing clearing solution, the sample was stained with DAPI and Poly T Reagent (Vizgen 20300021) for 15 minutes at room temperature, washed for 10 minutes with 5 ml of Formamide Wash Buffer, and then imaged on the MERSCOPE system (Vizgen 10000001). A fully detailed, step-by-step instruction on the MERFISH sample prep the full protocol is available at <https://vizgen.com/resources/fresh-and-fixed-frozen-tissue-sample-preparation/>. Full instrumentation protocol is available at <https://vizgen.com/resources/merscope-instrument/>.

For the MERFISH gene panel, we selected 1000 genes for MERFISH experiments. The panel includes major cell-type and subcluster markers, BBB-related genes, genes of LR pairs analyzed in this study (specifically major cell type to EC LR pairs, major cell type to mural cell LR pairs, and EC and mural cell subcluster LR pairs), and several chemokine-related and meninges-related genes. The detailed gene list is provided in [Table S6](#).

RNA amplification-based single molecule in situ hybridization (asmFISH) assay

The SEERNA® FISH RNA Fluorescence in Situ Hybridization Kit used in this experiment was purchased from Suzhou Dynamic Biosystems Co., Ltd., and its methodology followed previously described research.⁹⁰ We detected the expression of transporter genes in co-cultured human ECs and human ESC-induced NPCs/neurons. In brief, fresh cells were first fixed with 4% PFA, followed by dehydration through a graded ethanol series (70%, 85%, and 100%). Subsequently, the cells were permeabilized. Next, according to the manufacturer's instructions, the cells were subjected to the asmFISH in situ hybridization procedure, which included the following steps: probe hybridization, post-hybridization washing, probe circularization, rolling circle amplification and fluorescent probe hybridization. Finally, the slides were mounted with SlowFade Gold Antifade Mountant medium containing DAPI (Thermo Fisher Scientific, S36940). Fluorescence images were acquired by Zeiss LSM880.

Immunostaining

The tissue blocks were fixed in 4% PFA solution at 4 °C for 24 to 48 hours and then were dehydrated in 30% sucrose solution for 24 to 48 hours. Next, they were embedded in OCT and the frozen sections were cut with a thickness of 20 to 40 μ m. For immunostaining, the sections were fixed in 4% PFA solution for 20 min, and washed three times with 1% PBST (1% Triton X-100 in 1M PBS) solution for 10 min each time. The slices were then treated with Quick antigen repair solution for frozen sections (1X) (Beyotime, # P0090) at room temperature for 5 min. Thereafter, they were incubated in blocking solution (1% PBST supplemented with 5% BSA) for 1 hour at room temperature. The slices were incubated with the primary antibodies with the staining solution (1% PBST supplemented with 1% BSA) at 4 °C overnight. In the following day, the tissue sections were incubated with the fluorescent secondary antibodies and subjected to Confocal images with a Zeiss

LSM 880. The following antibodies were used: mouse anti-CD31 (1:1000, Abcam, Cat #: ab9498), guinea pig anti-CD31 (1:1000, Synaptic Systems, Cat #: HS-351004), rat anti-CD31 (1:1000, BD Biosciences, Cat #: 553370), rabbit anti-MFSD2A (1:1000, Cell Signaling Technology, Cat #: 80302S), rabbit anti-SLC1A4 (1:1000, Novus, Cat #: NBP2-38226), rabbit anti-ABCG2 (1:1000, Abcam, Cat #: ab207732), mouse anti-CLAUDIN5 (1:1000, Invitrogen, Cat #: 35-2500), rabbit anti-CADHERIN-2 (1:1000, Cell Signaling Technology, Cat #: 13116T), goat anti-SOX2 (1:1000, R&D Systems, Cat #: AF2018), mouse anti-TUJ1 (1:1000, Millipore, Cat #: MAB1637), rabbit anti-c-JUN (1:1000, Cell Signaling Technology, Cat #: 9165), mouse anti-Human NESTIN (1:1000, R&D, Cat #: MAB1259), rabbit anti-GLUT-1 (1:1000, Millipore, Cat #: 07-1401), goat anti-PDGFRB (1:100, R&D Systems, Cat #: AF385), rabbit anti-KI67 (1:1000, Abcam, Cat #: ab15580), rabbit anti-PDGFD (1:1000, Abcam, Cat #: ab181845), rabbit anti-TGFB1 (1:1000, Abcam, Cat #: ab215715), mouse anti-TGFBR2 (1:1000, Proteintech, Cat #: 66636-1-Ig), rabbit anti-ANGPT2 (1:1000, Abcam, Cat #: ab276042), rabbit anti-TIE2 (1:1000, Abcam, Cat #: ab24859), mouse anti-COL1A1 (1:1000, Proteintech, Cat #: 66761-1-Ig), rabbit anti-ITGB1 (1:1000, Atlas Antibodies, Cat #: HPA059297), rat anti-PDGFB (1:500, Abcam, Cat #: ab107101), mouse anti-INSR (1:1000, Invitrogen, Cat #: MA5-13783), rabbit anti-H2A.Z.1 (1:1000, Active Motif, Cat #: 39943), Isolectin B4 (1:1000, Fisher scientific, Cat #: NC9918852), rabbit anti-VEGFR2 (1:1000, Cell Signaling Technology, Cat #: 2479), rabbit anti- β -catenin (1:1000, Cell Signaling Technology, Cat #: 8480), rabbit anti-LEF1 (1:1000, Cell Signaling Technology, Cat #: 2230), rabbit anti-TCF1 (1:1000, Cell Signaling Technology, Cat #: 2203), rabbit anti-CAV-1 (1:1000, Cell Signaling Technology, Cat #: 3267).

Plasmid constructs

shRNAs for the target genes were cloned into the pSicoR-GFP vector. The sequences were as follows: human *CDH2* shRNA: 5'-GTGCAACAGTATACGTTAATA-3', human *PDGFD* shRNA: 5'-CGATGACTACTTTGTGGCTAA-3', mouse *H2afz* shRNA: 5'-GGTAAGGCTGGAAAGGACT-3',⁶⁵ mouse *Ctnnb1* shRNA: 5'-CCCAAGCCTAGTAAACATAA-3'.⁹¹ Mouse *Control*, *Pdgfd* and *H2afz*; and *Ctnnb1* were amplified by PCR and subcloned into the pCDH-copGFP-3Flag vector and the pCDH-copGFP-3HA vector, respectively.

Lentivirus packaging and infection

For lentivirus packaging and infection, the method was described in the previous study.⁹² In brief, using GenEscort® II (Nanjing Weisen Biotechnology Company, #: WIS 2200), lentivirus was achieved by transfecting the core and packaging plasmids into 293FT cells. After 24h, 48h and 72h of transfection, the supernatant was collected. To remove cell debris, the supernatant containing

the virus was centrifuged at 3000 rpm for 5 min. Meanwhile, to improve infection efficiency, 2 $\mu\text{g/ml}$ polybrene was added into the culture medium.

Human ESCs differentiation to human NPCs and Neurons

H9 human ESCs were fed fresh media daily and when the growth density reached 70%, the medium was replaced with neural differentiation medium. The medium was composed of 50% DMEM/F12 medium (Invitrogen, #: 11330-032), 50% Neurobasal medium (Invitrogen, #: 21103-049), 1 \times N-2 supplement (GIBCO, #: 17502-048), 1 \times B27 supplement without vitamin A (GIBCO, #: 12587010), 1 \times GlutaMAX (GIBCO, #: 35050061), 10 ng/ml human Leukemia Inhibitory Factor (hLIF) (Millipore, #: LIF1010), 2 μM dorsomorphin (Sigma-Aldrich, #: P5499), 3 μM SB431542 (Tocris Bioscience, #: 1614), 4 μM CHIR99021 (Stemgent, #: 04-0004-10) and 0.1 μM compound E (R&D Systems, #: 6476). Fresh medium was replaced every other day. After 5 days, cells were digested into single cells with Accutase (Thermo Fisher Scientific, #: A1110501) and maintained in Matrigel-coated plates in Neural Progenitor Cell Maintenance Medium, which was composed of 50% DMEM/F12 medium, 50% Neurobasal medium, 1 \times N-2 supplement, 1 \times B27 supplement, 2 mM GlutaMAX, 10 ng/ml hLIF, 2 μM SB431542 and 3 μM CHIR99021. For neuronal differentiation, after maintained on Matrigel-coated plates for 2 days, NPCs were cultured in DMEM/F12 medium containing 1 \times N-2 supplement, 1 \times B27 supplement, 200 μM ascorbic acid (Sigma-Aldrich, #: A8960), 400 μM dbcAMP (Selleck, #: S7858), 10 ng/ml GDNF (Peprotech, #: 450-10) and 10 ng/ml BDNF (Peprotech, #: 450-02). Cells were maintained in the above medium for 7 days and used for subsequent experiments.

Co-culture of human ECs and human ESC-induced NPCs/ neurons

After infecting human ESC-induced NPCs/ neurons with lentivirus for 2 days, the hCMEC/D3 cells were added and co-cultured 3 days (human NPC/human neuron medium: human EC medium = 2:1) for subsequent experiments.

In utero electroporation with PDGFD knockdown or overexpression and PDGFR inhibitor treatment

The experimental procedures were performed as previously described. Briefly, control or overexpression plasmid (approximately 1500 ng/ μL) were mixed with enhanced GFP plasmid at a 3:1 ratio (v/v). For experiment of PDGFD overexpression and PDGFR inhibitor treatment, the plasmid mixture was then combined with PBS or PDGFR inhibitor (Selleck, CP-673451, 0.5 mg/mL) at a 9:1 ratio (v/v), followed by addition of 0.02% Fast Green (Millipore). The final solution was aspirated into glass capillaries for subsequent use. Pregnant ICR mice at embryonic day 13.5 (E13.5) were anesthetized via intraperitoneal injection of tribromoethanol (400 mg/kg). The abdominal cavity was surgically opened to expose the uterus. Approximately 1 μL of the mixed plasmid solution was microinjected into the lateral ventricle of fetal brains using glass capillaries. Electroporation was immediately performed on the fetal brains using a manual BTX ECM 830 electroporator with platinum electrodes, applying five electrical pulses at 40 V (50 ms pulse duration, 950 ms intervals). The uterine horns were carefully repositioned into the abdominal cavity. Embryonic brains were harvested at embryonic day 16.5 (E16.5) for further phenotypic analysis.

Pericytes proliferation assay with human NPCs supernatant

Firstly, we infected human ESC-induced NPCs with lentivirus. After 48 hours, the supernatant was collected and divided into two portions: one portion was used for ELISA, while the other portion was concentrated 10-fold using ultrafiltration tubes, mixed with pericytes culture medium at a 1:3 (v/v) ratio, and subsequently employed for pericyte culture. After 48 hours, the cells were fixed with paraformaldehyde for the next experiment.

Pericytes proliferation assay with PDGFD and PDGFR inhibitor treatment

First, pericytes were seeded in 24-well plates. When reaching 20% confluency, the supernatant was removed. One treatment group was supplemented with PDGFD^{93,94} (MCE, HY-P7280; 50 ng/ml) in pericyte culture medium, while the other treatment group with both PDGFD (50 ng/ml) and a PDGFR inhibitor (CP-673451, Selleck, S1536; 416 ng/ml).⁹⁵ The control group was treated with an equivalent volume of PBS in normal culture medium. After 48 hours of culture in their respective media, the cells were harvested for subsequent experiments.

Enzyme linked immunosorbent assay (ELISA)

PDGFD protein levels in the supernatant of human ESC-induced NPCs infected with lentivirus were measured using a human PDGFD ELISA Kit (Abelbio, AE28224HU) according to the manufacturer's instructions.

Transmission electron microscopy

P14 mice were administered horseradish peroxidase (HRP, 40 mg/ml, dissolved in PBS, Sigma-Aldrich, P8250) via retro-orbital injection at a dose of 0.5 mg/g body weight. After 1 hour of circulation,⁹⁶ brains were harvested and fixed sequentially in phosphate buffer (PB) (0.1 M, pH 7.4) containing 4% PFA and 5% glutaraldehyde for 3 hours, followed by post-fixation in 4% PFA overnight. Tissues were rinsed in PBS overnight and sectioned into 80- μm -thick free-floating coronal slices using a vibratome (Leica VT1200S). Sections were incubated at room temperature for 45 minutes in 0.05 M tris-HCl buffer (pH 7.6) containing 3,3'-diaminobenzidine (DAB, 0.5 mg/ml; Sigma-Aldrich, D8001) and 0.01% hydrogen peroxide. For mice without HRP injection, embryonic brains were collected immediately after euthanasia. Tissues were fixed with 2.5% (v/v) glutaraldehyde and 2% paraformaldehyde (v/v) in PB (0.1 M, pH 7.4), and dissected into small blocks without DAB staining. Then, the samples were washed two times in PB and two times

in ddH₂O. Then samples were first immersed in 1% (w/v) OsO₄ and 1.5% (w/v) potassium ferricyanide aqueous solution at 4°C for 2 h. After washing, tissues were dehydrated through graded alcohol (30%,50%,70%,80%,90%, 100%, 100%, 10min each) into pure acetone (two times, 10 minutes each). Samples were infiltrated in graded mixture (3:1, 1:1, 1:3, v/v) of acetone and SPI-PON812 resin (SPI-PON812: DDSA: NMA, 49: 16.5: 34.5, v/v/v), then changed pure resin. Finally, tissues were embedded in pure resin with 1.5% BDMA and polymerized for 12h at 45°C, 48 h at 60°C. The ultrathin sections (70nm thick) were sectioned with microtome (Leica, EM UC6), picked upon 100-mesh formvar/carbon-coated copper grids, double-stained by uranyl acetate and lead citrate, and examined by a transmission electron microscope (FEI Tecnai Spirit120kV) with the EMSIS CCD camera (VELETA).

Embryonic BBB permeability assay

First, for the injection of cadaverine-555 (Invitrogen, a30677) assay, we referred to published research.^{14,97} For E15.5 fetal mice, we performed laparotomy on E15.5 pregnant *H2afz^{fl/fl}* female mice (mated with *H2afz^{fl/+ (Tek-Cre)}* male mice) after anesthesia, and opened the uterus of the female mice to expose the fetal mice. Next, we retained the umbilical cord to supply blood to the fetal mice, and then used a microsyringe to inject 10μl cadaverine-555 (1mg/ml, dissolved in PBS) into the fetal liver of the mice. After 3 minutes of blood circulation, we collected the brains of the fetal mice.

Second, for the injection of EZ-link Sulfo-NHS-LC-Biotin (Thermo Fisher Scientific, A39257) assay, the method was referenced from previous study.¹⁴ For E15.5 fetal mice, we performed laparotomy on E15.5 pregnant *H2afz^{fl/fl}* female mice (mated with *H2afz^{fl/+ (Tek-Cre)}* male mice) after anesthesia, and opened the uterus of the female mice to expose the fetal mice. 25μl EZ-link Sulfo-NHS-LC-Biotin (4 mg/ml, dissolved in PBS) was injected into the fetal liver of the mice. After 10 minutes of blood circulation, the brains of fetal mice were collected and utilized for subsequent experiments.

Postnatal BBB permeability assay

P2 mice were injected 25μl cadaverine-555 (1 mg/ml, dissolved in PBS) into the abdominal cavity, and after 2 hours of blood circulation, the brains were collected for further experiments.⁹⁷

P7 mice were administered 25μl EZ-Link Sulfo-NHS-LC-Biotin (4 mg/ml, dissolved in PBS) via injection of left ventricle with a microsyringe. After 8 minutes of circulation, brains were collected for subsequent experiments.¹⁴

Glutamine metabolism and homeostasis assay

40μl Glutamine-Cy3 (RuixiBio, R-R-0213, 2 mg/ml, dissolved in PBS) was injected into the abdominal cavity of P2 mice, after 2 hours of circulation, the brains were collected for further experiments.

Immunoprecipitation

For immunoprecipitation, the co-transfected bEnd.3 cells were sonicated in RIPA buffer (Solarbio) containing 1× protease inhibitor and centrifuged at 12,000 rpm for 15 minutes. Protein lysates from co-transfected cells were incubated with anti-Flag-tag or anti-HA-tag magnetic beads overnight at 4°C. Then, the magnetic beads were washed 6 times with pre-cooled washing buffer and boiled for 2 minutes with 1× loading buffer. The supernatant was used for next experimental analysis.

Western blotting

For western blotting of immunoprecipitation, the supernatant was separated with SDS/PAGE gel. And for western blotting of E15.5 cerebrovascular vessels in *H2afz^{fl/fl}* and *H2afz^{cKO (Tek)}* mice, ECs digested and FACS-purified as described in the previous section were sonicated in RIPA buffer (Solarbio) containing protease inhibitor and centrifuged at 12,000 rpm for 15 minutes. The lysates were separated on SDS/PAGE gels. Proteins in gel were transferred onto nitrocellulose (NC) or polyvinylidene fluoride (PVDF) membrane. The membrane was blocked with PBST (0.05% Tween20 in 1× PBS) containing 5% milk for 1 h at room temperature and incubated with primary antibodies overnight at 4°C. On the next day, the membrane was washed three times with PBST, each time for 10 minutes and incubated with fluorescent conjugated secondary antibodies at room temperature for 1 h. The fluorescence intensity of protein was scanned with an Odyssey fluorescent scanner.

Chromatin immunoprecipitation (ChIP)

The protocols were performed as previously described.⁹⁸ Briefly, the bEnd.3 cells were co-infected with lentivirus for 12 h and replaced with fresh culture medium. Three days later, the cells were crosslinked with 1% formaldehyde at room temperature for 10 minutes, and the reaction was stopped with 2.5M glycine. Then the cells were washed twice with cold PBS and homogenized in buffer 1 (50 mM pH 7.5 HEPES-KOH, 10% glycerol, 0.25% Triton, 0.5% NP-40, 140 mM NaCl, 1 mM EDTA, and 1× protease inhibitors) on a shaking table at 4°C for 10 minutes. The samples were centrifugated at 4000 rpm at 4°C for 5 minutes before discarding the supernatant and resuspended in buffer 2 (10 mM pH 8.0 Tris-HCl, 200 mM NaCl, 0.5 mM EGTA, 1 mM EDTA, and 1× protease inhibitors) on a shaking table at 4°C for 10 minutes. Next, the samples were centrifugated at 4000 rpm at 4°C for 5 minutes before discarding the supernatant and sonicated in lysis buffer 3 (50 mM pH 8.1 Tris-HCl, 1% SDS, 10 mM EDTA, and 1× protease inhibitors) using a sonicator (Scientz-IID, 15% power, ultrasonic treatment for 10 seconds, pause for 10 seconds) for 20 minutes. Then, the samples were centrifuged at 12000 rpm for 10 minutes and the supernatant was incubated with 50 μl Protein A/G magnetic beads (Invitrogen) with 2 μg pre-coupled antibodies at 4°C for 12 h. The magnetic beads were washed three times with low-salt buffer (pH 8.1 Tris-HCl, 0.1% SDS, 1% Triton X-100, 150 mM NaCl, and 2 mM EDTA) and three times with high-salt buffer (pH 8.1 Tris-HCl, 0.1% SDS, 1% Triton

X-100, 500 mM NaCl, and 2 mM EDTA). Finally, chromatin complexes were eluted from the magnetic beads with TES buffer (50 mM pH 8.0 Tris-HCl, 1% SDS, and 10 mM EDTA) at 65°C for 12 h. The DNA was purified using a TIANamp Genomic DNA Kit (Tiangen) and performed real-time PCR with a 7500 real-time PCR system (Applied Biosystems). The primers that were used for ChIP-qPCR were listed in [Table S7](#)

QUANTIFICATION AND STATISTICAL ANALYSIS

scRNA data processing

The raw reads files were processed using Cell Ranger (v5.0.1) by aligning reads to hg38 genome (GRCh38-2020-A) or mm-10 genome (mm-10-2020-A) to obtain gene counts matrix. For quality control, cells 1) with a high ratio of mitochondrial genes (more than 20%); 2) less than 500 or over 7,000 detected genes; 3) less than 1,000 or over 30,000 detected counts were filtered in Seurat (v4.3.0).¹ DoubletFinder (v2.0.3)² was used to remove potential doublets with default parameters for each sample. After filtering the outliers, 82,887 cells were obtained for human samples and 48,636 cells for mouse samples. The further downstream analyses were performed in Seurat. The NormalizeData function was used to normalize the count data with "LogNormalize" method. The top 2,000 variable genes were used to perform principal component analysis. RunHarmony function from Harmony (v0.1.0)³ was used to correct batch-effect from different samples. Dimensional reduction was performed using the RunUMAP function with the first 30 dimensions. Clusters of cells were identified by FindClusters function and marker genes of each cluster were found by FindAllMarkers function with default parameters. Cell types were manually annotated using known cell-type-specific marker genes. The endothelial cells, mural cells, neural progenitor cells and neuron cells were re-clustered and specific cell types were also identified based on classic marker genes. CellCycleScoring function was used to calculate cell cycle score for each cell and G2/M score was shown for each cell.

Spatial stereo-seq data pre-processing

The pre-process of raw reads files from Stereo-seq was followed by the previous publication.¹⁰ We also used bin50 for further analysis. The lasso tool from StereoMap (v2.1.0) (<https://www.stomics.tech/products/BioinfoTools/OfflineSoftware/list.html>) was used to get the coordinates of cerebral cortex and lasso tool from SAW (v.6.1)¹¹ was used to obtain the genes expression matrix. Then the genes expression matrix was converted to a Seurat object for the downstream analyses. And we used NormalizeData function to normalize the raw matrix with normalization.method = "LogNormalize" and scale.factor = 10,000.

Mapping cell types from scRNA-seq onto scStereo-seq

To identify the cell types of spatial transcriptomic data, we applied Tangram¹² to align our single-cell clusters to spatial data, computing a probabilistic spatial profile for each cell type. Specifically, we selected cell type marker genes ([Table S3](#)) that had a specific expression pattern in both scRNA-seq data and scStereo-seq data as the training genes. Before mapping, single-cell data was randomly extracted based on cell type proportions to reduce the impact of excessive cell proportions on the results. And then we used map_cells_to_space function with mode = "clusters" to project single cell data to space and project_cell_annotations function to project cell annotations to spatial data. Ggplot2¹³ package was used to visualize the spatial data.

MERFISH data preprocessing and mapping cell types from scRNA-seq onto MERFISH

Cell segmentation of MERFISH data was performed using Cellpose (v2.2.3)⁸⁷ from Vizgen Post-processing Tool (<https://github.com/Vizgen/vizgen-postprocessing>). Firstly, we used MERSCOPE Visualizer to select regions of the tissue to extract images to manually annotate. Secondly, Cellpose2 UI was used to annotate cell boundaries for the selected image patches based on nuclear staining (DAPI) and cytosolic staining (Poly T). Thirdly, we retrained the base model with the manual annotations and then re-segmented the original images using the refined model.

For downstream analysis, we filtered cells with fewer than 5 genes and segmentation volume less than 20 μm^3 and removed the outliers using the function from Voyager (v1.8.1)⁸⁸ package.

Next, we employed Tangram to map our single-cell data to MERFISH data at cluster level, enabling the identification of cell types, consistent with the approach used for the scStereo-seq data. The visualization of MERFISH data was performed using the relevant functions from Voyager package.

Correlation Analysis

For the correlation analysis between biological replicate samples for different datasets, we first identified variable features using the FindVariableFeatures function from Seurat. We then calculated the average expression of these genes in each sample using the AverageExpression function. The Pearson correlation coefficients between samples were also computed using cor function and visualized the results with Pheatmap.

Blood-brain barrier markers were used to analyze the correlation of endothelial cells between human and mouse. In brief, we used AverageExpression from Seurat to calculate the averaged expression values of blood-brain barrier markers for each identity class. And then used cor function from R⁹ with default parameter to compute the correlation. Pheatmap (v1.0.12) (<https://github.com/raivokolde/pheatmap>) package was used to visualize the result.

Enrichment analysis

Metascape⁴ was used to perform gene ontology enrichment analysis with input species set to *Homo sapiens* and using standard parameters.

Gene expression pattern analysis

The heatmap of the expression pattern of the genes of interest was created using the DoHeatmap function from Seurat, and the color scheme was adjusted according to the scaled gene expression level. The VlnPlot and Dotplot function from Seurat were used to generate an expression violin or dot plot of relevant genes across groups.

Gene expression quantification methods for scRNA-seq data

The dataset from Wälchli et al.⁷ was normalized using the LogNormalize method implemented in the Seurat package. As described in their methods: “we performed the standard Seurat clustering (version 4.0.0 in R 4.2.2) workflow, as described below; raw expression values were normalized and log transformed (normalization.method = ‘LogNormalize’).” Similarly, the dataset from Kalucka et al.¹⁶ was also normalized using the NormalizeData function in Seurat, as stated in their methods: “The data were normalized using the NormalizeData function as implemented in the Seurat package.” In our study, both the human and mouse datasets were processed and normalized using the same LogNormalize approach in Seurat.

Cluster ratio analysis

The bar chart of cluster ratio in different groups was created by dittoSeq (v1.6.0)⁵ package. The ggplot2⁶ package was used to generate the line chart that illustrates how the cluster ratio varies over the course of various development stages.

Trajectory analysis

Pseudotime trajectory analysis of human endothelial cells was performed using Monocle2 (v2.14.0).⁵ Specifically, gene counts matrix and cell types from Seurat were used to create a new CellDataSet object by newCellDataSet function. The top 600 cluster markers calculated by FindAllMarkers function from Seurat were used for ordering cells in pseudotime. “DDRTree” method was used to run dimensionality reduction. The differentiation trajectory was inferred by orderCells function by using state one as the root state. Differential expression analysis among the pseudotime was run by differentialGeneTest function with the default parameters. The expression pattern of the DEGs was shown using plot_genes_branched_heatmap function.

Analysis of public scRNA-seq datasets

Single-cell dataset of endothelial cells from developing adult human brain with cluster information was download from published data.^{7,30} For mouse brain endothelial cells, gene expression matrix was downloaded from ArrayExpress (accession number: E-MTAB-8077)¹⁶ and further processed as described above.

Correlation Analysis

For the correlation analysis between biological replicate samples for different datasets, we first identified variable features using the FindVariableFeatures function from Seurat. We then calculated the average expression of these genes in each sample using the AverageExpression function. The Pearson correlation coefficients between samples were also computed using cor function and visualized the results with Pheatmap.

The correlation analysis between scStereo-seq and MERFISH datasets. To assess transcriptional similarity between the scStereo-seq and MERFISH datasets at the global expression level, we performed a pseudobulk-based cross-platform correlation analysis. For each dataset, raw UMI counts were aggregated across within each sample to generate pseudobulk expression profiles. Only genes detected in both platforms were retained. To minimize differences in library size and gene detection sensitivity, pseudobulk counts were normalized using counts-per-million (CPM) followed by log(1+CPM) transformation. The platform-specific batch effects were corrected using ComBat function from sva (v3.54.0)⁹⁹ package. The Pearson correlation coefficients were then computed using cor function and visualized the results with corrplot (0.95) function.

Blood-brain barrier markers were used to analyze the correlation of endothelial cells between human and mouse. In brief, we used AverageExpression from Seurat to calculate the averaged expression values of blood-brain barrier markers for each identity class. And then used cor function from R⁹ with default parameter to compute the correlation. Pheatmap (v1.0.12) (<https://github.com/raivokolde/pheatmap>) package was used to visualize the result.

Cell-cell communication analysis

We used CellChat (v1.1.3)⁶ to infer cell-cell communication networks across all big cell types and all subclusters. Firstly, identify OverExpressedGenes and identifyOverExpressedInteractions function were used to identify over-expressed signaling genes and over-expressed ligand-receptor interactions. For big cell types, computeCommunProb function with raw.use = TRUE, population.size = TRUE, type="truncatedMean" and trim = 0.5 was used to calculate communication probability between all big cell types. For subclusters, computeCommunProb function with raw.use = TRUE, population.size = TRUE, type="truncatedMean" and trim = 0.25 was used to infer ligand-receptor interactions between subclusters. Next, we filtered cell-cell communication with minimum 5 cells in each cell group and compute the communication probability on signaling pathway level with default parameters. Finally, we visualized

the communication probabilities of pathways and ligand-receptor pairs by using the `netAnalysis_signalingRole_heatmap` and modified `netVisual_chord_gene` function from CellChat.

BBB scores

The expression of BBB related genes, including tight junction genes and transport genes (Table S5) were used to calculate module scores for ECs of scRNA-seq data, scStereo-seq data and MERFISH data by `AddModuleScore` function from Seurat. The results of scRNA-seq data were visualized using box plot, the results of scStereo-seq data were visualized using point plot (bin50), and the results of MERFISH data were visualized using scatter plot of cells to display the score of ECs. We also calculated the score proportions of different brain regions at each developmental stage using different thresholds.

Cell-cell communication in spatial transcriptomics data

COMMOT (v 0.0.3)³⁵ was adopted to infer cell-cell communication for MERFISH data. Briefly, we used the ligand-receptor database from CellChat and then performed spatial communication inference by using `spatial_communication` function with 500 μm spatial distance. The signaling direction was computed by `communication_direction` function with default parameters. The cell-cell communication score of interacting cell types was calculated by summing the interaction scores of the corresponding cells.

Cross-species analysis of endothelial cells

In order to explore the similarity of endothelial cells between human and mouse, the mouse endothelial cells were randomly extracted based on the sample to make the number of endothelial cells approximately equal to the number of human endothelial cells. Briefly, `FindIntegrationAnchors` function was applied to find a set of anchors between human and mouse endothelial cells. And computed anchorset was used to perform dataset integration using `IntegrateData` function with `dims = 1:10`. The first 5 dimensions after running principal component analysis were used as input to run uniform manifold approximation and projection for visualizing data.

Comparison of pseudotime trajectories between human and mouse

We used CAPITAL (v1.1.2)⁵⁶ to compare pseudotime trajectories with tree alignment between human and mouse. Firstly, `mousipy` (v0.1.5) (<https://github.com/stefanpeidli/mousipy>) package was used to translate mouse gene symbols to human gene symbols. Secondly, we calculated a trajectory tree for each species by setting early vein cells as the root node. And then the alignment of the two trajectory trees was run by `tree_alignment` function with default parameters. The similarity of gene expression dynamics between human and mouse was computed by `genes_similarity_score` with `min_disp = 0.5`.

Confocal imaging and statistical analysis

All the images were obtained by Zeiss LSM880 and processed with Photoshop CC 2021 (Adobe). The fluorescence density was calculated with Zeiss ZEN 2012 (blue version) and Imaris 9.0. Vascular indexes were analyzed using Imaris 9.0. Quantitative data was analyzed by two-tailed unpaired t test and showed as the mean \pm s.e.m. n.s., not significant; *P < 0.05; **P < 0.01; ***P < 0.001. All statistical analyses were conducted using GraphPad Prism 9.0.